Deficiency of mitophagy mediator Parkin in aortic smooth muscle cells exacerbates abdominal aortic aneurysm

Hui Wang[1,2,7], Matthew Kazaleh[2], Rachel Gioscia-Ryan[3], Jessica Millar[2], Gerard Temprano-Sagrera[4], Sherri Wood[1], Fran Van Den Bergh[5], Muriel G. Blin[1], Kathleen M. Wragg[1], Adrian Luna[1], Robert B. Hawkins[2,6], Scott A. Soleimanpour[1,5], Maria Sabater-Lleal[4], Chang Shu[7], Daniel A. Beard[5], Gorav Ailawadi[2,6], Jane C. Deng[8,9], Daniel R. Goldstein[6,9], and Morgan Salmon[2,6,10]

[1] Department of Internal Medicine, University of Michigan, Ann Arbor, Michigan, USA.

[2] Department of Cardiac Surgery, University of Michigan, Ann Arbor, Michigan, USA.

[3] Department of Anesthesiology, University of Michigan, Ann Arbor, Michigan, USA.

[4] Unit of genomics of Complex Diseases, Institut de Recerca Sant Pau (IR SANT PAU), Sant Quintí 77-79, 17 08041 Barcelona, Spain

[5] Department of Molecular and Integrative Physiology, University of Michigan, Ann Arbor, Michigan, USA.

[6] Frankel Cardiovascular Center, University of Michigan School of Medicine, Ann Arbor, Michigan, USA.

[7] Department of Vascular Surgery, The Second Xiangya Hospital, Central South University, Changsha, China.

[8] Pulmonary Division, University of Michigan, Ann Arbor, Michigan, USA.

[9] Veterans Affairs Ann Arbor, Ann Arbor, Michigan, USA.

[10]Corresponding author: Morgan Salmon, msalmon@med.umich.edu

2800 Plymouth Road, Ann Arbor, Michigan 48109 USA.

24 Word count**:** 12091

25 Running Title: Parkin SMCKO exacerbates AAAs

26

27 **Abbreviations:** AAAs, abdominal aortic aneurysms; AngII, angiotensin II; mtDAMPs,
28 mitochondrial damage – associated molecular patterns; EVAR, endovascular aneurysm repair
29 surgery; VSMCs, vascular smooth muscle cells; mtDNA, mitochondrial DNA; HFD, high-fat diet;
30 DMSO, dimethylsulfoxide; IP, intraperitoneal; MFI, mean fluorescence intensity; PKO, Parkin
31 knock-out; TPM, transcripts per million; BP, biological process; CC, cellular component; MF,
32 molecular function; DEG, differentially expressed genes; Parkin SMCKO, Parkin knock-out in
33 smooth muscle cells; RBC, red blood cells; WT, wild-type; USP30i, USP30 inhibitor; shRNA,
34 short hairpin RNA; SEM, standard error of the mean.

Abstract

Abdominal aortic aneurysms (AAAs) are a degenerative aortic disease and associated with hallmarks of aging, such as mitophagy. Despite this, the exact associations among mitophagy, aging, and AAA progression remain unknown. In our study, gene expression analysis of human AAA tissue revealed downregulation of mitophagy pathways, mitochondrial structure, and function-related proteins. Human proteomic analyses identified decreased levels of mitophagy mediators PINK1 and Parkin. Aged mice and, separately, a murine AAA model showed reduced mitophagy in aortic vascular smooth muscle cells (VSMCs) and PINK1 and Parkin expression. Parkin knockdown in VSMCs aggravated AAA dilation in murine models, with elevated mitochondrial ROS and impaired mitochondrial function. Importantly, inhibiting USP30, an antagonist of the PINK1/Parkin pathway, increased mitophagy in VSMCs, improved mitochondrial function, and reduced AAA incidence and growth. Our study elucidates a critical mechanism that proposes AAAs as an age-associated disease with altered mitophagy, introducing new potential therapeutic approaches.

1. Introduction

An abdominal aortic aneurysm (AAA) is defined as a local enlargement of the infrarenal aorta, with a global prevalence of 0.92% in individuals aged 30-79, which then escalates to 1.2%-3.3% in individuals over 60 years old [1, 2]. AAAs are currently understood to be an irreversible and progressive aortic dilation with the potential to rupture, which carries a mortality rate over 81%[3]. Other risk factors for AAAs include smoking, genetics, and sex. Men are at four times the risk of developing AAA compared to women, while women experience faster aneurysm growth and have a fourfold higher risk of rupture[1]. Currently, effective clinical management relies on open surgical repair or less invasive endovascular aneurysm repair (EVAR)[4]. Clinical trials investigating the potential of statins, antihypertensives, doxycycline, and anti-inflammatory medications as alternatives or adjuncts to surgical or endovascular treatment have yet to yield definitive efficacy[5-9]. Therefore, studies exploring the pathogenesis of AAAs, identifying potential new pharmacologic targets, are crucial for advancing current clinical management.

Vascular smooth muscle cells (VSMCs) constitute the predominant cellular population within the aortic wall, playing a pivotal role in the pathogenesis of AAAs. Their contribution to AAA development is characterized by a loss of contractile phenotype, increased apoptosis, immune cell recruitment, extracellular matrix remodeling, and enhanced oxidative stress[10]. Additionally, these adverse alterations are more pronounced in aged VSMCs and could describe potential mechanisms for the increased susceptibility of elderly populations to AAAs[11, 12]. However, definitive studies investigating the causal role of aging in AAA progression currently remain unexplored and largely unknown.

Emerging evidence indicates that mitochondrial dysfunction and aberrant mitochondrial dynamics are associated with the pathogenesis of AAA. For example, damaged mitochondria

release double-stranded mitochondrial DNA (mtDNA) into the cytosol, stimulating the downstream cGAS-STING, a critical innate immune pathway, promoting AAA development[13]. Separate studies demonstrated that mitochondrial fission, regulated by DRP1, is significantly increased in AAA tissues, and inhibition of DRP1 mitigates AAA progression[14]. Finally, decreased mitochondrial biogenesis, regulated by PGC1-α, has been identified in human and mouse aneurysm tissues when compared to health vascular tissue[15]. These studies suggest that the processes that regulate mitochondrial turnover and dynamics may be important in AAA progression. As a part of mitochondrial dynamics, mitophagy, a macro-autophagy that selectively degrades damaged mitochondria, is essential for mitochondrial quality control and hemostasis[16]. Recent evidence suggests that mitophagy mitigates inflammation triggered by the activation of the cGAS-STING pathway by mtDNA[17]. Given that reduced mitophagy is a hallmark of aging, and considering AAA's prevalence in older populations, investigating mitophagy's impact on AAA progression could represent a promising avenue for further understanding mechanisms of AAA formation or rupture[18, 19].

Previous studies, especially in Parkinson’s disease, have investigated the ubiquitin-mediated mitophagy pathway facilitated by mitochondrial kinase PINK1 and cytosolic E3 ubiquitin ligase Parkin [20, 21]. In detail, PINK1 accumulates on the outer mitochondrial membrane in damaged mitochondria with reduced membrane potential, where it recruits and phosphorylates Parkin. Activated Parkin ubiquitinates various mitochondrial membrane proteins, which are then recognized by autophagy receptors. These receptors facilitate the recruitment of LC3-decorated phagophores, leading to the encapsulation of the damaged mitochondria and subsequent fusion with lysosomes for degradation [22]. Mutations in *PINK1* or *PARK2* genes are associate with defective mitochondrial dysfunction and numerous studies suggest that targeting

95 the PINK1/Parkin pathway could be effective in preventing and treating cardiovascular diseases
96 [23, 24]. However, its role in the pathogenesis of AAAs has never been explored. USP30 is a
97 deubiquitinase localized to the mitochondrial outer membrane which antagonizes PINK1/Parkin
98 mediated mitophagy [25]. Inhibition of USP30 has been shown to enhance PINK1/Parkin-
99 mediated mitophagy [26]. Given the availability of a USP30 inhibitor, VB-08, exploring the role
100 of PINK1/Parkin-mediated mitophagy in the development of AAAs holds promise for identifying
101 potential pharmacological targets.

102 In this study, we tested our hypothesis that Parkin-mediated mitophagy is a critical factor
103 in the pathogenesis of AAAs. Our results demonstrate that genes related to the mitophagy pathway,
104 as well as genes involved in mitochondrial structure and function, were downregulated in human
105 AAA samples, coinciding with decreased protein expression of PINK1 and Parkin. Additionally,
106 we observed reduced mitophagy in VSMCs in advanced-aged murine aortas and in young murine
107 AAAs, both associated with decreased PINK1 and Parkin expression. Furthermore, Parkin
108 knockout in VSMCs resulted in more severe AAA rupture and increased aortic diameter, whereas
109 administration of a USP30 inhibitor, VB-08, reduced AAA incidence and diameter. Our findings
110 suggest that PINK1/Parkin-mediated mitophagy represents a potential novel therapeutic target for
111 AAA treatment.
112

113 **2. Material and Methods**

114 *2.1 Ethics statement*

115 Mice were housed and maintained at 70°F, 50% humidity, in 12-hour light-dark cycles per
116 institutional animal protocols. Animal care and use were in accordance with the Guide for the Care
117 and Use of Laboratory Animals. The animal protocol was approved by the University of Michigan

Institutional Animal Care and Use Committee (PRO00010704) in compliance with the Office of Laboratory Animal Welfare. The authors declare that all supporting data are available within the article and its online supplementary files but can provide additional information upon request to corresponding author.

2.2 Mice.

WT young (8-12 weeks) and aged (18-20 months) male C57BL/6J mice were obtained from The Jackson Laboratory (stock #000664). mito-QC mice, mitophagy reporter mice on the C57BL/6J background were generously provided by Dr. Ian Ganley and originally generated by Taconic Artemis[27]. These mice were bred and aged to the indicated age under specific pathogen free conditions in the animal facility at the University of Michigan. C57BL/6J Parkinfl/fl mice were a gift from the lab of Dr. Scott Soleimanpour, originally generated by Dr. Ted Dawson and Lexicon Genetics, with loxP sites flanking exon 7 of the Prkn allele [28]. C57BL/6J *Parkin*$^{fl/fl}$ mice were bred to *Myh11-cre/ER*^{T2} (stock #019079, C57BL/6 background), which were purchased from The Jacson Laboratory. 6-10 weeks *Parkin*$^{fl/fl}$ *Myh11-cre/ER*^{T2} mice received five daily intraperitoneal injections (i.p.) of either tamoxifen, to induce gene deletion, or vehicle (corn oil) and then rested for nine days. The outcomes of *Parkin*$^{fl/fl}$ *Myh11-cre/ER*^{T2} mice were evaluated alongside their vehicle-treated litter-mate controls. We used male mice to for conduct the research, as a significant body of studies has focused on males in AAA. This choice is supported by two key reasons. First, like humans, male mice exhibit a four-fold higher prevalence of AAA when infused with Angiotensin II compared to females [29], offering consistent and reproducible results with an optimal sample size. Second, the widely used *Myh11-cre/ER*^{T2} is carried on the Y chromosome and

140 effective for gene deletion only in male mice [30]. All the mice were maintained on a 12-h light-
141 dark cycle and had unrestricted access to food and water.
142
143 *2.3 Angiotensin II infusion AAA model.*
144 We employed an abdominal aortic aneurysm model combined with a PCSK9 gain-of-function
145 mutation with Angiotensin II infusion [31-34]. The PCSK9 gain of function mutation is induced
146 using a single intraperitoneal injection of recombinant adeno-associated virus 8-D377Y-murine
147 PCSK9 (PCSK9-AAV) at a dose of 5.0×10^9 vector genomes per gram body weight purchased from
148 the University of Pennsylvania Vector core. The mice were then fed ad libitum a high-fat diet (42%
149 calories from fat, HFD, Teklad, catalog #88137) for 6 weeks. Starting on the third week, mice
150 received subcutaneous infusion of Angiotensin II (Sigma, catalog #A9525) or saline at a rate of
151 1000 ng/kg/min using mini osmotic pumps (Alzet, model #1004) for the subsequent four weeks
152 [35].
153
154 *2.4 Elastase application AAA model.*
155 As a secondary model for AAA, periadventitial elastase was applied following established
156 methods[36, 37]. Male *Parkinfl/fl Myh11-cre/ER^{T2}* mice received a series of injections of either
157 corn oil (control, n=10/group) or tamoxifen (n=11/group) at 6-8 weeks of age. One month
158 following injection, the mice underwent a midline laparotomy to expose the infra-renal aorta,
159 which was then treated with full-strength elastase (Sigma, catalog #E1250). Each surgeon
160 determined the optimal elastase dose and duration through a pre-experimental dose-response curve,
161 reliably producing a 110% increase in aortic diameter in control mice. Fourteen days post-
162 operatively, the infra-renal abdominal aortas were harvested from both groups. During the harvest,

the abdominal aorta was exposed similarly, and maximal aortic diameters were measured using video micrometry. To calculate the percentage of diameter dilation, a specific section of the aorta not exposed to elastase served as an internal control.

2.5 USP30 inhibitor studies.

For C57/B6 male mice (n=25/group) receiving either VB-08 (25 mg/kg, i.p., daily, Vincerebio.com) or a vehicle (confidential, i.p., daily, Vincerebio.com). Treatment began nine days after the initiation of PCSK9 AAV and a HFD, and five days before the implantation of an Angiotensin II pump. The treatment continued for the following 5 days and 4 weeks during the induction of abdominal aortic aneurysm (AAA), or until the mice succumbed to aneurysm rupture within this period. Mice were harvested, and anatomical pictures were taken. Tissues were processed according to experimental purposes.

2.6 Cholesterol and blood pressure measurements.

Serum cholesterol levels in fasting mice were determined using a colorimetric assay (Cell Biolabs, catalog #STA-384). Blood pressure in mice was obtained using the CODA® non-invasive blood pressure system (Kent Scientific Corporation) via the tail-cuff method.

2.7 Aortic aneurysm assessments (rupture and diameters).

Following the implantation of the Angiotensin II pump, autopsies were conducted on mice that were found deceased. Deaths due to aortic aneurysm rupture were noted for inclusion in survival curve analysis. Four weeks post-implantation, mice were euthanized with CO_2 and a thoracotomy was performed. Blood was collected from the right ventricle, and the mice were perfused with cold

186 PBS through the left ventricle after opening the right atrium. The abdominal cavity was then
187 opened, and visceral organs were removed. The fat tissue and connections around the entire aorta
188 and adjacent heart were isolated under a dissecting microscope. Aortas with aneurysms were
189 identified under the microscope, and the corresponding mice were documented. The entire murine
190 aorta and adjacent heart were isolated and pinned to the wax-coated base of a Petri dish alongside
191 a ruler for scale. Photographs were taken, and the absolute value of maximal diameters of the aortic
192 aneurysms were measured using ImageJ software (National Institutes of Health, USA).
193
194 *2.8 Isolation and culture of primary aortic VSMCS.*
195 Vascular smooth muscle cells (VSMCs) were extracted from the abdominal aortas of 5-week-old
196 male mito-QC mice using an enzymatic digestion method. Following euthanasia, the aorta was
197 dissected under sterile conditions. The fatty and adventitial layers were removed through an 8–10-
198 minute digestion with an enzyme cocktail consisting of 1 mg/ml collagenase type II (Worthington
199 Biochemical Corp, catalog #LS004176), 1 mg/ml soybean trypsin inhibitor (Worthington
200 Biochemical Corp, catalog #LS003570), and 0.744 units/ml elastase (Worthington Biochemical
201 Corp, catalog #LS002279), all at 37°C in a 5% CO2 atmosphere. The aortas were then
202 longitudinally sliced open and rinsed three times to remove the endothelial cell layer. These aortas
203 were then segmented into 1-2 mm pieces and incubated in a fresh enzyme cocktail at 37°C in 5%
204 CO2 for one hour. Post centrifugation, the resulting pellet was resuspended and cultured in VSMC
205 media composed of 10% FBS (Gibco, catalog #16000044), 100 unit/ml penicillin and 100ug/ml
206 streptomycin (Gibco, catalog #15140122) in DMEM/F12(Gibco, catalog #11320033). The media
207 was refreshed every 2-3 days, and cells were passaged upon reaching approximately 80%
208 confluence. Cells were utilized up to the eighth passage.

209

210 *2.9 Cell culture, pharmacological intervention and Lentiviral shRNA transduction.*

211 MOVAS (ATCC, catalog #CRL-2797) were cultured in DMEM/F12 (Gibco, catalog #11320033)
212 supplemented with 10% FBS (Gibco, catalog #16000044), 100 unit/ml penicillin and 100ug/ml
213 streptomycin (Gibco, catalog #15140122) at 37°C in 5% CO2. Cells were passaged at 80%
214 confluence. MOVAS and VSMCs were starved in DMEM/F12 containing 0.2% FBS for 48 hours
215 and then received 100nM, 500nM or 1000nM Angiotensin II (Sigma, catalog #A9525) for an
216 additional 48 hours. The USP30 inhibitor was administered at concentrations of 100nM, 200nM,
217 500nM or 1000nM, either concurrently with or 24 hours prior to the Angiotensin II treatment.
218 Particularly, to assess mitophagy level changes in MOVAS cells, Mtphagy dye (Dojindo, catalog
219 # MT02-10) was incubated for 30 minutes prior to any pharmacological intervention, in
220 accordance with the manufacturer's protocol.

221

222 Lentiviral shRNA targeting Parkin (Santa Cruz, catalog #sc-42159-V) and control shRNA particles
223 (Santa Cruz, catalog #sc-108080) were purchased from Santa Cruz Biotechnology. Transduction
224 and selection of transduced cells were performed according to the manufacturer's protocol. Briefly,
225 MOVAS cells were seeded in 12-well plates and cultured to 70-80% confluence. Cells were then
226 transduced with Parkin shRNA or control lentiviral particles at a multiplicity of infection (MOI)
227 of 0.25, 0.5, or 1, in the presence of 5 μg/mL polybrene (Santa Cruz, catalog #sc-134220).
228 Following overnight incubation, the medium was replaced with fresh complete media, and cells
229 were incubated for an additional 24 hours. To select stably transduced cells, the cultures were split
230 and maintained in complete medium supplemented with 2 μg/mL puromycin (Santa Cruz, catalog

231 #sc-108071) for 7 days, with medium changes every 2-3 days. Surviving cells were then expanded
232 for further experimentation. Knockdown efficiency was confirmed by Western blot analysis.
233
234 *2.10 MitoSOX Red, MitoTracker, and TMRM staining in cells.*
235 After Angiotensin II treatment, cells were detached using 0.05% Trypsin-EDTA (Gibco, 25300054)
236 and collected. LIVE/DEAD^{TM} Aqua (Thermo Scientific, catalog #L34957) staining was performed
237 for 5 minutes. Subsequently, cells were incubated with 5μM MitoSOX Red (Thermo Scientific,
238 catalog #M36008) or 25nM MitoTracker Deep Red (Thermo Scientific, catalog #M22426) along
239 with 100nM TMRM (Thermo Scientific, catalog #I34361) in a dark environment at 37°C.
240 Following incubation, cells were washed, and flow cytometry acquisition using a ZE5 Cell
241 Analyzer was conducted immediately.
242
243 *2.11 Flow cytometry.*
244 For the cellular samples requiring staining with MitoSOX Red, MitoTracker or TMRM, cells were
245 processed and stained according to method *2.10*. Subsequently, flow cytometric analysis was then
246 conducted using a ZE5 Cell Analyzer (Bio-Rad). For the murine aortic samples processing, aortas
247 were isolated following PBS perfusion and then slightly sectioned longitudinally into strips. These
248 tissue strips were then enzymatically digested into single-cell suspensions using a cocktail
249 containing 3.2mg/ml collagenase Type II (Worthington Biochemical Corp, catalog #LS004176),
250 0.7mg/ml elastase (Worthington Biochemical Corp, catalog #LS002279), 0.2mg/ml soybean
251 trypsin inhibitor (Worthington Biochemical Corp, catalog #LS003570) in RPMI 1640(Gibco,
252 catalog #11875093) at 37°C. The digestion took 30 minutes and was facilitated by intermittent
253 pipetting. The resulting cell suspension was filtered through a 70μm mesh. Red blood cells were

254 lysed using a 2-minute incubation with RBC lysis buffer (BioLegend, catalog #420302) and the
255 cells were then washed. For staining, cells were first labeled with LIVE/DEAD™ Aqua for
256 viability assessment for 5 minutes, followed by a 5-minute incubation with Fc blocking reagent,
257 anti-mouse CD16/32 (BioLegend, catalog #101320). A cocktail of surface antibodies was then
258 applied for 30 minutes, including Brilliant Violet 785™ CD31 antibody (BioLegend, catalog
259 #102435), APC CD90.2 (Thy-1.2) antibody (BioLegend, catalog #140312) and Alexa Fluor® 700
260 CD45 antibody (BioLegend, catalog #103128). After surface staining, cells were fixed,
261 permeabilized using BD Cytofix/Cytoperm™ (BD Biosciences, catalog #555028), and stained
262 with intracellular antibody for α-actin (Invitrogen, catalog #14-9760-82) and subsequent
263 secondary antibody (BioLegend, catalog #405317) for 30 minutes each. Flow cytometric data
264 acquisition was again performed on a ZE5 Cell Analyzer (Bio-Rad). All the data analysis was
265 conducted by FowJo™ Software_v10.9.0 (Ashland, 2023).
266
267 *2.12 Western blotting of MOVAS and aortic tissues.*
268 Cellular and aortic tissue proteins were extracted using RIPA buffer (Sigma-Aldrich, catalog
269 #R0278) supplemented with 1% protease inhibitor (Sigma-Aldrich, catalog #P8340) and
270 phosphatase inhibitor (Sigma-Aldrich, catalog #P5726). Protein concentration was determined by
271 the BCA protein assay per manufacturer's protocol (Thermo Scientific, catalog #23225). Equal
272 amounts of protein (20-25mg) were separated onto a 10% Nupage SDS-PAGE gels (Thermo
273 Scientific, catalog #NP0315BOX, NP0303BOX) and then transferred to PVDF membranes
274 (Thermo Scientific, catalog #IB24001) through semi-dry method. Membranes were blocked in 5%
275 BSA (Gemini Bio-Products, catalog #700-100P) in 0.1% TBST for 1 hour at room temperature,
276 then incubated with primary antibodies overnight at 4°C on a shaker. After washing, the

277 membranes were incubated with HRP-conjugated secondary antibodies (abcam, catalog
278 #ab205718, ab205719) for 1 hour at room temperature. Bands were visualized using enhanced
279 chemiluminescence (Thermo Scientific, catalog #34580, 34094) and captured with ChemiDoc MP
280 imaging system (Bio-Rad). Band intensity was quantified with ImageJ software and normalized to
281 Vinculin, β-tubulin or GAPDH. All the antibodies used here are listed in supplementary table 1.
282
283 *2.13 Frozen section and mitophagy measurement of GFP and mCherry fluorescence.*
284 Aortic segments were harvested and immersed in 3.7% paraformaldehyde within 200 mM HEPES
285 buffer for overnight fixation. Subsequently, the fixed tissues were cryo-preserved in OCT
286 compound (Sakura, catalog #4583) and sectioned into 6 μm slices using a Leica Cryostat (model
287 CM1850-3-1). The sections were then placed on slides and sealed with Prolong Diamond mounting
288 media (Thermo Scientific, catalog #P36961). Imaging was conducted with a Nikon A1si confocal
289 microscope, utilizing a 100x magnification objective lens across both GFP and mCherry channels.
290 Quantitative analysis of mCherry puncta was performed using ImageJ software.
291
292 *2.14 qPCR analysis.*
293 RNA extraction from aortic tissue was conducted using the TRIzol-ethanol method. The
294 concentration of extracted RNA was determined using a NanoDrop spectrophotometer.
295 Subsequently, 1 μg of RNA was reverse transcribed into cDNA using the iScript cDNA Synthesis
296 Kit (Bio-Rad, catalog #1708891). TaqMan primers, obtained from Thermo Fisher Scientific, were
297 employed for qPCR, which was performed according to the TaqMan Advanced Master Mix Kit
298 protocol (Applied Biosystems, catalog #4444557) on a QuantStudio 3.0 Real-Time PCR System.

299 Gene expression levels were quantified based on the fold change in Ct values. The details of the
300 primers used are listed in supplementary table 1.
301
302 *2.15 Immunohistochemistry and immunofluorescence.*
303 Aortic segments were harvested and immersed in a 4% paraformaldehyde buffer for overnight
304 fixation. Subsequently, the fixed tissues were dehydrated, cleared, embedded, sectioned, and
305 mounted on positive-charged slides. For the staining, tissue sections were deparaffinized and
306 hydrated. Endogenous peroxidase activity was quenched by hydrogen peroxide in methanol for 30
307 minutes. Antigen retrieval was performed using citrate buffer (pH 6.0, Vector, catalog #H-3300-
308 250) in a microwave for 20 minutes, followed by blocking non-specific binding with 10% horse
309 serum at room temperature. Supplementary table 2 lists all the antibodies used in the subsequent
310 steps. For immunohistochemistry, primary antibody was applied to the sections and incubated
311 overnight at 4°C. After washing by PBS, secondary antibody was applied to the sections and
312 incubated for 1 hour at room temperature. The signal was detected using DAB for 5-10 minutes.
313 Then the sections were counterstained by hematoxylin, dehydrated, cleared, and mounted with
314 Permount™ mounting media (Fisher Scientific, catalog #SP15-100). Images were captured and
315 quantification of staining intensity was performed using ImageJ software. For
316 immunofluorescence, primary antibodies conjugated with distinct fluorophores were applied to the
317 sections and incubated overnight at 4°C. After washing by PBS, sections were stained by DAPI.
318 These sections were then placed on slides and sealed with Prolong Diamond mounting media
319 (Thermo Scientific, catalog #P36961). Imaging was conducted with a Nikon A1si confocal
320 microscope, utilizing a 60x magnification objective lens across channels of DAPI, Alexa Fluor
321 488, 555 and 647.

322

323 *2.16 MitoSox Red staining for tissue.*

324 Aortic segments were excised and immediately snap-frozen in OCT compound (Sakura, catalog
325 #4583). The blocks were sectioned to a thickness of 6 µm and mounted onto slides. Sections were
326 rinsed with HBSS, followed by incubation in 5 µM MitoSox Red (Thermo Scientific, catalog
327 #M36008) for 1 hour at 37°C. After a subsequent wash with HBSS, slides were promptly imaged
328 using a Nikon A1si confocal microscope with a 100x magnification objective lens.

329

330 *2.17 Oxygraph analysis of murine aortas.*

331 Aortas were isolated and maintained in BIOPS buffer on ice, followed by permeabilization with
332 50 µg/ml saponin for 25 minutes, and subsequently rinsed in MiR05 for 10 minutes [38]. The wet
333 weights of the aortas were then blotted, measured, and documented. High-resolution
334 measurements of oxygen consumption in permeabilized aortic tissue were performed in 2 ml of
335 MiR05 buffer using the Oroboros Oxygraph-2k (O2k; Oroboros Instruments, Innsbruck, AT). The
336 oxygen consumption rate was determined from plateau values on the oxygraphy chart and
337 expressed as pmol s^{-1} per mg of wet weight. All measurements of respiration were carried out at
338 37 °C within an oxygen concentration working range of approximately 190-50 µM. As published
339 previously by our lab [39], the respiration process was assessed through sequential titrations of
340 substrates and inhibitors: 11.25 mM ADP (CalBiochem, catalog #117105), 0.5 mM malate (Sigma,
341 catalog #M1000), 5 mM pyruvate (Sigma, catalog #P2256), 10 mM glutamate (Sigma, catalog
342 #G1626), 10 mM succinate (Sigma, catalog #S2378, mentioned twice and may need correction),
343 0.5 µM CCCP (Sigma, catalog #C2759), 0.5 µM rotenone (Sigma, catalog #R8875), and 2.5 µM
344 antimycin-A (Sigma, catalog #A8674).

345

346 *2.18 Mitochondrial DNA copy numbers.*

347 Relative mtDNA copy numbers by qPCR with SYBR-based detection (Thermo scientific, catalog
348 #A46109) was conducted following DNA isolation with the Blood/Tissue DNeasy kit (Qiagen,
349 catalog #69504) according to manufacturer's protocols. Primer sequences: mt9/mt11 (5′-
350 GAGCATCTTATCCACGCTTCC-3′ and 5′- GGTGGTACTCCCGCTGTAAA-3′) for mtDNA
351 and Ndufv1 (5′- CTTCCCCACTGGCCTCAAG-3′ and 5′- CCAAAACCCAGTGATCCAGC-3′)
352 for nuclear DNA. The fold changes in mt9/mt11 expression were normalized to the Ndufv1 gene
353 [40].

354

355 *2.19 Metabolomics experiments and analysis.*

356 Targeted metabolomics analyses were performed as reported by Seals Laboratory and carried out
357 by the University of Colorado Metabolomics Core Facility[41], plasma (20 µL) were extracted in
358 1 mL of ice-cold lysis/extraction buffer (methanol:acetonitrile:water 5:3:2). After discarding
359 protein pellets, water and methanol soluble fractions were injected into a C18 reversed phase
360 column (phase A: water, 0.1% formic acid; B: acetonitrile, 0.1% formic acid - Phenomenex)
361 through an ultra-high performance chromatographic system (UHPLC, Ultimate 3000; Thermo
362 Fisher). UHPLC was coupled online with a high-resolution quadrupole Orbitrap instrument run in
363 either polarity modes (QExactive, Thermo Fisher) at 70,000 resolution (at 200 *m/z*). Maven
364 software (Princeton), KEGG pathway database, and an in-house validated standard library (>650
365 compounds; Sigma Aldrich; IROATech) were used for metabolite assignment and peak integration
366 for relative quantitation. Integrated peak areas were exported into Excel (Microsoft) and elaborated
367 for statistical analysis (*t* test, ANOVA) and hierarchical clustering analysis through the software

368 GraphPad Prism (GraphPad Software) and GENE E (Broad Institute). Top up- and down-regulated
369 metabolic pathways were determined through MetaboAnalyst 3.0
370 (www.metaboanalyst.ca/MetaboAnalyst/).
371
372 *2.20 Analysis of Bulk RNA Sequence data.*
373 For our team's dataset, the expression values used in these plots correspond to the residuals
374 obtained from a linear regression with gene expression that included all covariates except the
375 disease variable (AAA/control). Gene quantifications were expressed as transcripts per million
376 (TPM), normalized via quantile normalization. Prior to differential expression analysis, genes with
377 low expression levels, defined as TPM values below 0.5 in more than 50% of the samples, were
378 excluded. To identify differentially expressed genes between AAA and controls, a linear regression
379 model was employed, incorporating a number of covariates, including age, sex, flow cell type,
380 flow cell lane, mean GC content, RIN, percentage of RNA fragments > 200 and Qubit. The p-
381 values obtained from the regression were corrected using the Benjamini-Hochberg procedure, and
382 a gene was considered to be differentially expressed if the adjusted p-value was less than 0.05.
383 Samples were clustered into a heatmap by mitophagy-related genes, including "ATG7",
384 "MAP1LC3B", "AMBRA1", "OPTN", "USP30", "BNIP3", "BNIP3L", "PHB2", "PINK1",
385 "FUNDC1", "ATG5", "BECN1", "PARK2", "PPARGC1A".
386 We also analyzed one published AAA dataset, Erik et al. (GEO accession number, GSE 57691),
387 with 20 small and 49 large human AAA samples and 10 donor samples in this cohort. The
388 normalization was applied using limma package. Principal Component Analysis was performed to
389 facilitate clustering of the samples. Outliers were identified and removed. The data matrices were
390 annotated using attached gene symbols. Matrix file was obtained for analyzing Differentially

391 Expressed Genes (DEGs), with |log2FC| > 0.8 and an adjusted p-value < 0.05. Genes were
392 matched with human genes in org.Hs.eg.db. Then GO and KEGG enrichment analysis were
393 conducted. Dot plot and gene-concept network plot were plotted. Finally, samples were clustered
394 into a heatmap by available mitophagy-related genes, including "ATG7", "MAP1LC3B", "OPTN",
395 "USP30", "BNIP3", "BNIP3L", "PHB2", "FUNDC1", "ATG5", "BECN1", "PPARGC1A".
396
397 *2.21 Statistics***.**
398 All results are presented as mean ± standard error of the mean (SEM). Normality was determined
399 using Shapiro-Wilk test. Nonparametric tests were used for data that were not normally distributed.
400 Data with one independent variable were analyzed using Student's t test or Mann-Whitney U-test.
401 When more independent variables were analyzed, one-way ANOVA or 2-way ANOVA with
402 multiple comparisons were used. Specific statistical tests and *P values* are denoted in figure
403 legends. Two-sided *P values* were used and values <0.05 were considered significant. GraphPad
404 Prism 10.0.0 (GraphPad Software) was used to generate figures and for statistics.
405
406 **3. Results**
407 *mito-QC aged mouse aortas demonstrate decreased mitophagy in VSMCs and endothelial cells*
408 *and a reduction of PINK1/Parkin expression.*
409 Previous studies have demonstrated decreased mitophagy in aged brain and heart tissue, as
410 well as reduced Parkin levels in aged aortas [42-44]. Despite this, changes in mitophagy levels
411 within aged aortic tissue and AAAs have not been explored. We utilized flow cytometry to analyze
412 digested aortas from young (8-10 weeks) and aged (18-20 months) male mito-QC mice using a
413 previously published staining strategy [45] (Fig. 1A, Supplementary Fig. S1A). As gating strategy

414 showed, endothelial cells were identified as $CD45^{-}CD31^{+}$ cells, general $CD45^{+}$ cells were
415 identified as $CD31^{-}CD45^{+}$ cells, and VSMCs as $CD45^{-}CD31^{-}CD90^{-}\alpha\text{-actin}^{+}$ cells (Supplementary
416 Fig. S1A). Plots comparing GFP and mCherry fluorescence across three cellular populations
417 revealed a decrease in GFP levels in $CD45^{+}$ cells from aged aortas and in VSMCs from young
418 aortas. (Fig. 1B). Mitophagy levels were quantified by the mean fluorescence intensity (MFI) of
419 mCherry versus GFP for each group as reported previously by our lab [46]. In endothelial cells,
420 aged mice exhibited a significant decrease in mitophagy of approximately 5%, in both thoracic
421 and abdominal aortic segments compared to young mice (Fig. 1C). Conversely, the $CD31^{-}CD45^{+}$
422 cellular population showed a significant increase in mitophagy levels in aged mice (Fig. 1C).
423 Finally, there was a notable decrease in mitophagy levels of approximately 10%, in the VSMCs of
424 the thoracic and abdominal aged aortic segments (Fig. 1C).

425 Western blot analyses of mitophagy-related pathways in the aged aortas demonstrated
426 significant decreases in PINK1 and Parkin expression, whereas changes in Nix and PHB2 were
427 not significant (Fig. 1D, E). Additional mitophagy biogenesis markers, including PGC1α and Paris,
428 and autophagy-related markers LC3II and MTOR, also showed significant reduction via Western
429 blot (Fig. 1D, E). However, the mitochondrial fission marker DRP1 and mitochondrial complexes
430 remained unchanged between young and aged aortas (Fig. D, E, Supplementary Fig. S1B, C). On
431 the other hand, VDAC1, an internal control for mitochondrial complexes, demonstrated a
432 significant decrease in the aged aorta. The specificity of Parkin was further validated in brain and
433 aortic tissues of WT versus Parkin knockout mice (Supplementary Fig. S1D).

434

435 *Reduction of Mitophagy in VSMCs in Angiotensin II induced AAAs*

436 We next sought to determine whether AAA induction alters mitophagy using mito-QC male
437 mice in three groups: male mice on a chow diet with saline pump, male mice on HFD with saline
438 pump, and male mice on HFD with AngII infusion at 1000 ng/kg/min. In the HFD/AngII AAA
439 model, serum cholesterol levels gradually increased over a 4-week HFD period (Supplementary
440 Fig. S2A). Mice were harvested 28 days posted AngII infusion, cells were stained as previously
441 mentioned, and flow cytometry was conducted as in Figure 1 (Fig. 2A). The gating strategy was
442 consistent with Figure 1 and adjusted for VSMCs which were categorized into $CD45^{-}CD31^{-}CD90^{-}$
443 $\alpha\text{-actin}^{high}$ and $CD45^{-}CD31^{-}CD90^{-}\alpha\text{-actin}^{low}$ groups, due to altered expression of α-actin in the
444 AAA (Supplementary Fig. S2B-C) [45]. $\alpha\text{-actin}^{high}$ and $\alpha\text{-actin}^{low}$ VSMCs from the HFD plus
445 AngII group exhibited significantly reduced mitophagy levels compared to the HFD plus saline
446 group (Fig. 2B, C), whereas endothelial cells and $CD31^{-}CD45^{+}$ immune cells showed no
447 significant changes (Fig. 2B). In separate studies, mice on an AngII pump without HFD also
448 displayed markedly lower mitophagy in VSMCs compared to Saline pump without HFD
449 (Supplementary Fig. S2D). Additionally, analysis of frozen aortic sections revealed fewer mCherry
450 puncta and reduced colocalization of LAMP-1, a lysosomal marker, and TOMM20, a
451 mitochondrial marker, in the HFD plus AngII group compared to those on HFD plus saline (Fig.
452 2D, E and F).

453 The previous studies demonstrated decreased mitophagy levels in the VSMCs in AAAs
454 following AngII infusion; therefore, we sought to investigate the potential involvement of the
455 PINK1/Parkin-mediated mitophagy pathway in AAAs. qPCR analysis demonstrated Parkin
456 (*Park2*), and α-actin (*ACTA2*) were significantly downregulated in AAA specimens, while *PINK1*,
457 *MYH11*, and other autophagy markers demonstrated no significant changes (Fig. 3A). Western blot
458 analysis noted Parkin and PINK1 were substantially reduced within murine AAAs, whereas PHB2

459 increased significantly, and Nix remained largely unchanged following HFD and AngII treatment
460 (Fig. 3B, C). Additional Mitochondrial biogenesis and autophagy markers analyzed noted with a
461 reduction in PGC1α, increases in STING, TBK1 and LC3II, alongside a decrease in α-actin in
462 murine AAAs (Fig 3B, C). The downregulation of Parkin and α-actin was further corroborated by
463 IHC staining, with markedly diminished signals in the aortic medial layer (Figure 3D, E and
464 Supplementary Fig. S2C). Furthermore, Western blot analysis confirmed a reduction in SDHB, a
465 complex II protein, in HFD plus Ang II infusion along with a decreasing trend observed for ATP5A
466 in complex V and NDUFB8 in complex I (Fig. 3F, G).
467
468 *Human AAA samples exhibit decreased expression of mitophagy mediator Parkin and PINK1 in*
469 *gene and protein level.*
470 The expression of mitophagy-related genes was analyzed in our bulk RNA-seq dataset,
471 which included 44 control samples and 96 AAA samples (Fig. 4A). PINK1 exhibited a significant
472 decrease in the AAA group and PARK2 showed a decreasing trend. Similarly, USP30, an
473 antagonist of the PINK1/Parkin mitophagy pathway, also exhibited a decreasing trend. Mediators
474 of other mitophagy pathways, such as BNIP3 and BNIP3L, were downregulated, but PHB2
475 expression remained unchanged. For generic autophagy mediators, MAP1LC3B and ATG7 were
476 upregulated, whereas ATG5 showed no significant change. Regulators of the mitophagy pathway,
477 including AMBRA1, BECN1, FUNDC1, and OPTN, were decreased in the AAA group. The
478 mitochondrial pathogenesis-related gene, PPARGC1A, showed no change.
479 In this dataset, the control and AAA groups could not be distinctly clustered based on these
480 mitophagy-related genes (Supplementary Fig. S3A). In the publicly available dataset GSE57691,
481 a clearer distinction between the control and AAA groups was observed using available mitophagy-

482 associated genes (Supplementary Fig. S3B). KEGG pathway enrichment analysis (Supplementary
483 Fig. S3C) indicated that genes involved in biological processes such as aerobic respiration, the
484 electron transport chain, oxidative phosphorylation, ATP synthesis coupled with electron transport,
485 and the mitochondrial ATP synthesis coupled electron transport and aerobic electron transport
486 chain were downregulated in the AAA group. Additionally, genes associated with cellular
487 components, including the respirasome, respiratory chain complex, and mitochondrial respirasome,
488 were downregulated. Genes related to molecular functions, such as electron transfer activity and
489 antioxidant activity, were also downregulated.

490 A gene-concepts plot revealed that the observed decreases in ATP synthesis coupled with
491 electron transport and the electron transport chain were primarily due to downregulated proteins
492 in the mitochondrial complex, which were also associated with the response to peptide hormones
493 via gene CYC1 (Supplementary Fig. S3D). In our human bulk RNA-seq dataset, a significant
494 downregulation of nuclear genes encoding mitochondrial complexes I-V (Supplementary Fig.
495 S3E-I) and mitochondrial ribosome components (Supplementary Fig. S3J-K) was observed in the
496 AAA samples. Protein expression analysis demonstrated that Parkin was significantly decreased
497 in the AAA samples, with PINK1 also showing a decreasing trend. There were no significant
498 changes in STING, Nix, and the LC3II/I ratio (Fig. 4B-C).

499

500 *Parkin SMCKO mice have increased propensity for AAA rupture and an augmented maximal*
501 *diameter of the aneurysm, concomitant with enhanced mitochondrial dysfunction.*

502 Given reduced mitophagy levels in VSMCs in AAAs and reduced Parkin expression in the
503 aortic medial layer following AngII infusion, we next sought to examine effects of cell specific
504 Parkin elimination in VSMCs in AngII AAAs. We utilized *Myh11-creER*^{T2}*Parkin*$^{fl/fl}$ in an

505 HFD/AngII-induced AAA model [28, 30], by administering either vehicle (Control) or tamoxifen
506 (Parkin SMCKO) followed by AAA induction (Fig. 5A). Verification of Parkin knockout in
507 VSMCs was confirmed through genotyping of tail samples and Western blot analysis of the mouse
508 aorta (Supplementary Fig. S4A, B). Prior to AngII pump implantation, the Parkin SMCKO group
509 exhibited significantly lower serum cholesterol levels and weight gain compared to the control
510 group; however, no differences in cholesterol or weight gain were observed at the time of harvest
511 6 weeks following tamoxifen administration (Supplementary Fig. S4C, D). Following AngII
512 infusion, aortic ruptures were confirmed by autopsy and were included as a death event in the
513 survival analysis. The Parkin SMCKO group exhibited lower survival rates (7/39 Parkin SMCKO
514 versus 1/35 WT; p=0.0383), a trend toward greater aneurysm incidence (p=0.066), and increased
515 maximal aortic diameters compared to WT controls (Fig. 5B, C). In the elastase-induced AAA
516 model, increased aortic dilation was also observed in the Parkin SMCKO group compared to the
517 control group, with mean dilation percentages of 136.80 ± 20.80% versus 99.69 ± 22.33%
518 (p=0.0009; Supplementary Fig. S4E).

519 At the tissue level, less colocalization of LAMP1 and TOMM20 was observed in the Parkin
520 SMCKO group (Fig. 5D). Western blot analysis revealed an increase in STING protein levels and
521 an altered autophagy marker ratio of LC3II to LC3I in the Parkin SMCKO group (Fig. 5E, F).
522 Furthermore, Parkin SMCKO exhibited increased mitochondrial ROS, decreased mitochondrial
523 copy numbers (p=0.0260), and a trending decline in protein levels of ATP5A in complex V
524 (p=0.140), UQCRC2 in complex III (p=0.0701), and SDHB in complex II (p=0.1027; Fig. 5I-J).
525 The protocol employed for measuring oxidative phosphorylation (OXPHOS) capability in aortic
526 mitochondria is detailed schematically in Figure 5K [39], and demonstrated that the oxygen

527 consumption rate, both coupled and uncoupled for Complex I and II, was significantly reduced in
528 the Parkin SMCKO group compared to controls (Fig. 5L).
529
530 *Parkin SMCKO AAA mice exhibited metabolomic profiles with altered ATP synthesis, nucleotide*
531 *metabolism, increased oxidative stress, deficient fatty acid β-oxidation.*
532 Serum metabolomics analysis of control versus Parkin SMCKO groups following AngII
533 AAA formation was performed, and bioinformatics analyses was conducted. The scores plot (Fig.
534 6A) reveals a clear separation between the two groups, indicating significant metabolic differences
535 due to Parkin SMCKO. The heatmap, volcano plot, and analysis of individual metabolites (Fig.
536 6B, C and Supplementary Fig. S4F) show notable increases in phosphate and diphosphate levels,
537 suggesting alterations in ATP synthesis. Additionally, levels of UDP and xanthine were also
538 elevated, reflecting changes in nucleotide metabolism and increased oxidative stress. Elevated
539 acyl-C4-DC levels point to deficient fatty acid β-oxidation, while increased spermidine indicates
540 a compensatory response in autophagy. Metabolomic pathway analysis (Fig. 4P) also highlights
541 significant changes in metabolites involved in both glycolysis and the TCA cycle, including 2/3-
542 phospho-D-glycerate, 1,3-bisphospho-D-glycerate, and oxaloacetate.
543
544 *VB-08, a USP30 inhibitor, can improve the reduction in mitophagy, and mitochondrial dysfunction*
545 *caused by AngII in vitro, with effect dependent on Parkin.*
546 Primary VSMCs isolated from the aortas of mito-QC mice were treated with AngII at
547 varying concentrations with the proportion of lysosomal mitochondria, indicated by diminished
548 percentage of GFP signal, demonstrating a dose-dependent decrease following AngII treatment
549 (Fig. 7A). In separate studies, MOVAS cells treated with AngII exhibited an increase in

550 mitochondrial ROS that was not dose-dependent (Fig. 7B). In subsequent studies, when MOVAS
551 cells were co-treated with AngII and VB-08, a highly selective USP30 inhibitor small molecule
552 and enhancer of the PINK1/Parkin mitophagy pathway, the AngII-induced reduction in mitophagy
553 was significantly reversed (p=0.0004 AngII vs. AngII + VB-08; Fig. 7C). The co-treatment led to
554 a trend toward a reduction in mitochondrial ROS (p=0.0770; Fig. 7D). Concurrently, the MOVAS
555 cells displayed a decrease in total mitochondrial content but an increase in mitochondrial health,
556 as evidenced by the ratio of mitochondrial membrane potential (TMRM) to Mitotracker
557 fluorescence (Fig. 7E). Western blot analyses demonstrated that treatment with AngII notably
558 decreased Parkin expression, particularly at concentrations of 100 nM and 500 nM (Fig. 7F,
559 supplementary Fig. S5A, B). Conversely, treatment with VB-08 significantly increased the
560 expression of both PGC1α and Parkin (Fig. 7G). Protein expression analysis demonstrated that
561 Parkin was significantly decreased in the AAA samples, with PINK1 also showing a decreasing
562 trend. To demonstrate whether the protective effect of VB-08 is related to Parkin expression, we
563 used lentiviral Parkin shRNA to knock down Parkin protein in MOVAS by around 43%
564 (supplementary Fig. S5C, D). The cells were treated with AngII alone or in combination with VB-
565 08. In control (scrambled shRNA) and Parkin knockdown MOVAS, AngII increased mitochondrial
566 ROS levels and reduced the percentage of healthy mitochondria. While VB-08 was expected to
567 reduce ROS and promote the mitochondrial health, it left notably higher ROS levels and lower
568 percentage of healthier mitochondria in the Parkin knockdown MOVAS (Fig. 7H).
569

570 *Treatment with USP30 inhibitor* VB-08 *in vivo significantly reduced aneurysm incidence and*
571 *diameter and enhanced mitochondrial function.*

572 mito-QC mice, subjected to a HFD and AngII-induced AAA model, received either vehicle
573 or VB-08 treatment daily, starting five days before and continuing four weeks after AngII pump
574 implantation (Supplementary Fig. S6A). Subsequent flow cytometry analysis of harvested aortas
575 revealed an increase in mitophagy levels of VSMCs with VB-08 treatment (Supplementary Fig.
576 S6B). This regimen was replicated in C57BL/6 mice with the AAA model over the same duration
577 (Fig. 8A). Treatment with VB-08 and AngII infusion demonstrated no significant differences in
578 serum cholesterol levels between the two groups (Supplementary Fig. S6C) nor were there survival
579 differences (Fig. 8B). However, AAA incidence was significantly lower in the USP30 inhibitor
580 group compared to vehicle control (p=0.010; Fig. 8B) with a corresponding trend toward decreased
581 aneurysm diameter (p=0.0652; Fig. 8B, C). Protein expression analysis via Western blot in the
582 aorta indicated a significant increase in PINK1 levels (p=0.0164) and the ratio of LC3II to LC3I
583 (p=0.0011) in the USP30 inhibitor group (Fig. 8D, E). While STING expression decreased
584 significantly (p=0.0208), Parkin expression exhibited a downward trend (p=0.0626; Fig. 8D, E).
585 Conversely, PGC1α levels trended upward (p=0.2976), with no notable changes in Nix and PHB2
586 expressions (Fig. 8D, E). mtDNA copy numbers in the aorta markedly increased in the USP30
587 inhibitor group (p=0.0426; Fig. 8F). Following the established protocol described for Parkin
588 SMCKO, both uncoupled and coupled oxygen consumption rates in complex I and II showed an
589 upward trend in the USP30 inhibitor-treated group, although no significant changes were observed
590 in complex content except that ATP5A in complex V showing an increasing trend (Figure 8G,
591 supplementary Fig. S6D, E).
592
593 *AAAs with USP30 inhibition exhibited metabolomics profile with altered ATP synthesis, energy*
594 *metabolism, neurotransmitter turnover, nucleotide metabolism, and decreased oxidative stress.*

595 Serum metabolomics analysis of the vehicle (control) and VB-08 groups, as demonstrated
596 by the scores plot (Fig. 9A), shows a clear separation between groups, indicating significant
597 metabolic differences due to VB-08 treatment. Metabolomic profiling, as depicted in the heatmap,
598 volcano plot, and individual metabolite analysis (Fig. 9B, C, and Supplementary Fig. S6F), reveals
599 distinct metabolic shifts. Decreased levels of phosphate and acyl-carnitine, which are involved in
600 ATP synthesis and fatty acid oxidation [47, 48], contrast with the trends observed in the Parkin
601 SMCKO intervention, highlighting a unique and connected metabolic response to USP30
602 inhibition and Parkin SMCKO. Notably, pyruvate and 2-oxoglutarate levels are reduced, while
603 fumarate is increased, indicating a shift in energy metabolism from glycolysis and the citric acid
604 cycle towards oxidative phosphorylation with VB-08 administration. Changes in lipid and
605 carbohydrate metabolism are suggested from decreased hexanoic acid and D-rhamnose, alongside
606 increased gamma-L-glutamyl-D-glucose and N-acetylneuraminic acid, reflecting adjustments in
607 fatty acid oxidation and glycosylation [49, 50]. Alterations in nucleotide and amino acid
608 metabolism are marked by decreased cytidine and hypoxanthine levels, coupled with increased
609 GMP and L-methionine, suggesting enhanced nucleotide synthesis, RNA production, and DNA
610 methylation (supplementary Fig. S6F) [51, 52]. Additionally, there are notable changes in
611 neurotransmitter-related metabolites, with decreased acetylcholine versus increased 5-
612 hydroxyindoleacetate and serotonin, indicating altered cholinergic and serotonergic dynamics.
613 Elevated levels of S-glutathionyl-L-cysteine, ascorbate, and Cys-Gly highlight an up-regulation in
614 antioxidant defenses and detoxification processes, reducing oxidative damage and supporting
615 cellular health (supplementary Fig. S6F) [53]. These findings are further corroborated by the
616 metabolomic pathway analysis (Fig. 9D), which underscores significant alterations across various
617 metabolic pathways, illustrating a broad metabolic reprogramming driven by USP30 inhibition.

618

619 **4. Discussion**

620 Recent evidence suggests that the dysregulation of mitochondrial quality control during
621 aging adversely affects mitochondrial function and may contribute to cardiovascular disease
622 progression [54, 55]. Evidence also suggests that mitophagy acts as a molecular sensor for the
623 maintenance of mitochondrial quality by clearing defective mitochondria. Although evidence
624 suggests decline in mitophagy levels is a hallmark of aging, alterations in mitophagy within
625 specific aortic cell types have not been reported. Our study shows that mitophagy declines in aged
626 murine aortas specifically in VSMCs ($CD90^{-}$α-$actin^{+}$) and endothelial cells ($CD31^{+}$), but not in
627 general immune cells ($CD45^{+}$). Furthermore, while it is known that the prevalence and severity of
628 AAA increases with advancing age, few studies have investigated Parkin-dependent mitophagy in
629 AAAs [15, 19]. Our findings reveal that mitophagy decline in VSMCs during AAA development
630 is associated with reduced expression of PINK1/Parkin-mediated mitophagy pathway in the aorta,
631 a known mitophagy regulatory pathway, in both murine and human AAAs. We demonstrated
632 Parkin SMCKO exacerbates murine AngII and elastase induced AAAs, leading to increased
633 severity of mitochondrial dysfunction and STING expression, underscoring the importance of
634 Parkin-mediated mitophagy in AAA. In contrast, enhancing the PINK1/Parkin-mediated
635 mitophagy pathway through USP30 inhibition significantly reduces AAA incidence, improves
636 mitochondrial function, and decreases STING expression, indicating that the PINK1/Parkin
637 mitophagy pathway is a promising therapeutic target for AAA. Our data suggest that enhancing
638 the PINK1/Parkin-mediated mitophagy pathway in VSMCs can improve AAA outcomes,
639 positioning it as a potential therapeutic avenue for this aging-related disease.

640 We initially identified decreased mitophagy levels in the VSMCs and endothelial cells of
641 aged murine aortas (20-month-old mito-QC mice), while general immune cells demonstrated
642 increased mitophagy levels. This increase in general immune cell mitophagy is logical considering
643 that senescent immune cells in aged aortas are more inflammatory, relying on the turnover of
644 defective mitochondria to facilitate inflammatory responses [56, 57]. Previous research using mt-
645 Keima mice reported increased overall aortic mitophagy in 16-month-old male mice, although
646 failed to distinguish cellular types [39]. Both mito-QC and mt-Keima mice are mitophagy reporter
647 tools that utilize pH-sensitive fluorescence detection. The fixable characteristic of mito-QC mice,
648 unlike the live-imaging feature of mt-Keima mice, gives mito-QC method the ability to measure
649 mitophagy levels in different cellular types following fixation. Previous studies have demonstrated
650 good coordination between these two tools for mitophagy measurements[58, 59]. Moreover, mito-
651 QC mice exhibit longer lifespans than mt-Keima mice, making them more applicable for *in vivo*
652 aging studies. Consistent with our results, Thomas et al. found reduced Parkin expression in the
653 aortas of 27-28-month-old mice, attributing this impairment to increased mitochondrial redox
654 stress and superoxide, which is also implicated in AAA pathogenesis [42, 60, 61].

655 Mitophagy in VSMCs is suggested to protect cells from apoptosis and oxidative stress
656 caused by cytochrome C release and damaged mitochondria [62]. Despite the verified importance
657 of autophagy in maintaining VSMC homeostasis in AAA, verified by Atg5 or Atg7 SMCKO
658 exacerbating AAA, little is known about the role of VSMC mitophagy during AAA development
659 [45, 63]. Our study demonstrates that mitophagy decline in VSMCs occurs during AAA
660 development and removal of Parkin within VSMCs increases AAA incidence. Furthermore, the
661 impaired mitochondrial respiratory function, decreased healthy mitochondria proportion, and
662 increased mitochondrial reactive oxygen species (mtROS) in Parkin SMCKO AAA underscore

663 Parkin's importance in AAA. Our current findings corroborate previous studies that demonstrated
664 decreased Parkin expression in human AAA samples compared to healthy controls [64].

665 The cGAS-STING pathway, activated by cytosolic DNA, including leaked mtDNA
666 segments, is known to partially prevent AAA development when inhibited [13]. Defective
667 mitophagy during aging has been shown to activate the mtDNA-related cGAS-STING pathway[17,
668 65, 66]. Our results show decreased PINK1 and Parkin expression alongside increased STING in
669 AAA samples. In Parkin SMCKO AAA, where mitochondrial dysfunction is more severe, STING
670 expression is further elevated, while enhancing PINK1/Parkin-mediated mitophagy through
671 USP30 inhibition decreases STING expression. This highlights a link between PINK1/Parkin-
672 mediated mitophagy and the STING-related innate immune pathway in AAA, providing additional
673 evidence for the investigation of mitophagy, aging, and STING interactions.

674 There is evidence suggesting crosstalk between different mitophagy mechanisms, although
675 the interplay remains to be further explored [67]. PHB2 and Nix are autophagy receptors located
676 at the inner and outer mitochondrial membranes, respectively, and traditionally viewed as
677 independent of the PINK1/Parkin pathway [68]. Our results suggest that Parkin expression
678 correlates with PHB2 but not with Nix. During AAA development, PHB2 expression significantly
679 increases while Parkin expression diminishes in AAA samples. In Parkin SMCKO AAA mice,
680 there is a trend of increasing PHB2 expression in aortic tissues. Recent research shows that PHB2
681 is essential for Parkin-mediated mitophagy and conversely, Parkin can directly interact with and
682 ubiquitinate PHB2 during mitophagy [69, 70]. Thus, our findings support a potential connection
683 between PHB2 and the PINK1/Parkin mitophagy pathway, warranting further investigation into
684 PHB2's impact on PINK1/Parkin-mediated mitophagy during AAA.

685 Metabolomic analysis of Parkin SMCKO AAA serum reveals increased Acyl-C4-DC, a
686 marker of deficient mitochondrial β-oxidation of fatty acids, potentially due to increased
687 mitochondrial dysfunction in the AAA tissue of Parkin SMCKO mice. These data are consistent
688 with previous findings that suggests synthetic VSMCs rely more heavily on fatty acid oxidation
689 than glucose oxidation [71].Conversely, USP30 inhibitor treatment elevates serotonin levels in the
690 serum. Recent studies indicate that serotonin enhances mitochondrial functions by increasing
691 mitochondrial respiration and membrane potential, impacting reactive oxygen species and
692 intracellular ATP [72]. Serotonin also regulates mitochondrial biogenesis via the SIRT1-PGC1α
693 axis [73]. While the role of serotonin in AAA is not yet investigated, its competing pathway, the
694 kynurenine pathway, is upregulated during AAA [74, 75]. Inhibition of Indoleamine 2–3
695 dioxygenase 1 (IDO), which converts tryptophan into the kynurenine pathway, has been shown to
696 improve AAA outcomes [76]. This implies that upregulating the tryptophan-serotonin pathway
697 might benefit AAA treatment, aligning with our findings that serotonin's role in AAA merits further
698 investigation.

699 USP30 antagonizes Parkin-mediated mitophagy, with studies showing that USP30
700 inhibition attenuates Parkinson's disease, subarachnoid hemorrhage induced early brain injury, and
701 kidney injury by inducing mitophagy [25, 77-79]; however, the role of USP30 in AAA remains
702 largely unexplored. Our *in vivo* and *in vitro* experiments demonstrate that USP30 inhibitor
703 treatment enhances Parkin-mediated mitophagy and PGC1α expression, promoting mitochondrial
704 biogenesis, and significantly reducing AAA incidence. The potential mechanism behind promoting
705 mitochondrial biogenesis could involve Parkin ubiquitinating PARIS, thus relieving its inhibition
706 of PGC1α transcription [80]. This evidence supports the notion that USP30 inhibition and

707 promotion of PINK1/Parkin-mediated mitophagy could be a promising therapeutic approach for
708 AAAs.

709 Our study has several limitations. Treating aged AAA mice with USP30 inhibitors would
710 enhance understanding, especially given the decreased baseline mitophagy levels in VSMCs from
711 aged aortas. However, aneurysm incidence is very low when applying the same AngII model to
712 aged mice, likely due to differences in aortic structure properties. Secondly, the designed
713 intervention aims to prevent rather than treat potentially influencing clinical translation. Thirdly,
714 the AngII and elastase AAA models do not fully represent human AAA pathogenesis and pathology;
715 thus, using additional complementary AAA models could further validate our results and would
716 represent potential future studies within this pathway. Future research could investigate potential
717 regulatory mechanisms of Parkin and PINK1 in the context of AAAs. There is limited evidence on
718 the upstream regulation of PINK1/Parkin, which remains to be explored. Research should also
719 explore Parkin's role in different cell types, as its function is suggested to extend beyond mitophagy
720 pathways due to its ability to ubiquitinate additional targets.

721 In conclusion, our study reveals a decline in mitophagy within aortic VSMCs during aging
722 and AAA formation, potentially linked to decreased PINK1/Parkin pathway activity. Parkin
723 SMCKO induces exacerbated AAA formation, while utilizing USP30 inhibitor to enhance
724 PINK1/Parkin-mediated mitophagy significantly reduces AAA incidence. The USP30 inhibitor,
725 which also possesses therapeutic potential in other degenerative diseases, holds promise as a novel
726 treatment for AAA.

727

728 **Acknowledgements** The USP30i molecule VB-08 was provided at no cost by Vincere
729 Biosciences Inc. (published in US Patent No. US11845724B2).

730 **Sources of Funding** This work was supported by NIH R35HL155169 and R01AI138347 (to
731 D.R.G.), and NIHR01AG028082 (to D.R.G. and J.C.D.).

732 **Disclosures** The authors of this manuscript have no conflicts of interest to disclose.

733

734 **References**

735 1. Song, P., et al., *The Global and Regional Prevalence of Abdominal Aortic Aneurysms:*
736 *A Systematic Review and Modeling Analysis.* Ann Surg, 2023. **277**(6): p. 912-919.
737 2. Force, U.S.P.S.T., et al., *Screening for Abdominal Aortic Aneurysm: US Preventive*
738 *Services Task Force Recommendation Statement.* JAMA, 2019. **322**(22): p. 2211-
739 2218.
740 3. Reimerink, J.J., et al., *Systematic review and meta-analysis of population-based*
741 *mortality from ruptured abdominal aortic aneurysm.* Br J Surg, 2013. **100**(11): p.
742 1405-13.
743 4. Isselbacher, E.M., et al., *2022 ACC/AHA Guideline for the Diagnosis and*
744 *Management of Aortic Disease: A Report of the American Heart*
745 *Association/American College of Cardiology Joint Committee on Clinical Practice*
746 *Guidelines.* Circulation, 2022. **146**(24): p. e334-e482.
747 5. Karlsson, L., et al., *The effect of azithromycin and Chlamydophilia pneumonia*
748 *infection on expansion of small abdominal aortic aneurysms--a prospective*
749 *randomized double-blind trial.* J Vasc Surg, 2009. **50**(1): p. 23-9.
750 6. Kiru, G., et al., *An evaluation of the effect of an angiotensin-converting enzyme*
751 *inhibitor on the growth rate of small abdominal aortic aneurysms: a randomised*
752 *placebo-controlled trial (AARDVARK).* Health Technol Assess, 2016. **20**(59): p. 1-180.
753 7. Propanolol Aneurysm Trial, I., *Propranolol for small abdominal aortic aneurysms:*
754 *results of a randomized trial.* J Vasc Surg, 2002. **35**(1): p. 72-9.
755 8. Baxter, B.T., et al., *Effect of Doxycycline on Aneurysm Growth Among Patients With*
756 *Small Infrarenal Abdominal Aortic Aneurysms: A Randomized Clinical Trial.* JAMA,
757 2020. **323**(20): p. 2029-2038.
758 9. Weaver, L.M., C.D. Loftin, and C.G. Zhan, *Development of pharmacotherapies for*
759 *abdominal aortic aneurysms.* Biomed Pharmacother, 2022. **153**: p. 113340.
760 10. Rombouts, K.B., et al., *The role of vascular smooth muscle cells in the development*
761 *of aortic aneurysms and dissections.* Eur J Clin Invest, 2022. **52**(4): p. e13697.
762 11. Li, M. and N.K. Fukagawa, *Age-related changes in redox signaling and VSMC*
763 *function.* Antioxid Redox Signal, 2010. **12**(5): p. 641-55.
764 12. Ungvari, Z., et al., *Mechanisms of Vascular Aging.* Circ Res, 2018. **123**(7): p. 849-
765 867.
766 13. Luo, W., et al., *Critical Role of Cytosolic DNA and Its Sensing Adaptor STING in*
767 *Aortic Degeneration, Dissection, and Rupture.* Circulation, 2020. **141**(1): p. 42-66.

14. Cooper, H.A., et al., *Targeting mitochondrial fission as a potential therapeutic for abdominal aortic aneurysm.* Cardiovasc Res, 2021. **117**(3): p. 971-982.
15. Wang, D., et al., *Mitochondrial quality control in abdominal aortic aneurysm: From molecular mechanisms to therapeutic strategies.* FASEB J, 2023. **37**(6): p. e22969.
16. Garbern, J.C. and R.T. Lee, *Mitochondria and metabolic transitions in cardiomyocytes: lessons from development for stem cell-derived cardiomyocytes.* Stem Cell Res Ther, 2021. **12**(1): p. 177.
17. Jimenez-Loygorri, J.I., et al., *Mitophagy curtails cytosolic mtDNA-dependent activation of cGAS/STING inflammation during aging.* Nat Commun, 2024. **15**(1): p. 830.
18. Chen, G., G. Kroemer, and O. Kepp, *Mitophagy: An Emerging Role in Aging and Age-Associated Diseases.* Front Cell Dev Biol, 2020. **8**: p. 200.
19. Ouyang, M., M. Wang, and B. Yu, *Aberrant Mitochondrial Dynamics: An Emerging Pathogenic Driver of Abdominal Aortic Aneurysm.* Cardiovasc Ther, 2021. **2021**: p. 6615400.
20. Liu, Y.J., et al., *Mitochondrial fission and fusion: A dynamic role in aging and potential target for age-related disease.* Mech Ageing Dev, 2020. **186**: p. 111212.
21. Corsa, C.A.S., et al., *The E3 ubiquitin ligase parkin is dispensable for metabolic homeostasis in murine pancreatic beta cells and adipocytes.* J Biol Chem, 2019. **294**(18): p. 7296-7307.
22. Ge, P., V.L. Dawson, and T.M. Dawson, *PINK1 and Parkin mitochondrial quality control: a source of regional vulnerability in Parkinson's disease.* Mol Neurodegener, 2020. **15**(1): p. 20.
23. Morais, V.A., et al., *Parkinson's disease mutations in PINK1 result in decreased Complex I activity and deficient synaptic function.* EMBO Mol Med, 2009. **1**(2): p. 99-111.
24. Wu, Y., et al., *PINK1/Parkin-mediated mitophagy in cardiovascular disease: From pathogenesis to novel therapy.* Int J Cardiol, 2022. **361**: p. 61-69.
25. Bingol, B., et al., *The mitochondrial deubiquitinase USP30 opposes parkin-mediated mitophagy.* Nature, 2014. **510**(7505): p. 370-5.
26. Okarmus, J., et al., *USP30 inhibition induces mitophagy and reduces oxidative stress in parkin-deficient human neurons.* Cell Death Dis, 2024. **15**(1): p. 52.
27. McWilliams, T.G., et al., *mito-QC illuminates mitophagy and mitochondrial architecture in vivo.* J Cell Biol, 2016. **214**(3): p. 333-45.
28. Von Coelln, R., et al., *Loss of locus coeruleus neurons and reduced startle in parkin null mice.* Proc Natl Acad Sci U S A, 2004. **101**(29): p. 10744-9.
29. Alsiraj, Y., et al., *Female Mice With an XY Sex Chromosome Complement Develop Severe Angiotensin II-Induced Abdominal Aortic Aneurysms.* Circulation, 2017. **135**(4): p. 379-391.
30. Wirth, A., et al., *G12-G13-LARG-mediated signaling in vascular smooth muscle is required for salt-induced hypertension.* Nat Med, 2008. **14**(1): p. 64-8.
31. Lu, H., et al., *Hypercholesterolemia Induced by a PCSK9 Gain-of-Function Mutation Augments Angiotensin II-Induced Abdominal Aortic Aneurysms in C57BL/6 Mice-Brief Report.* Arterioscler Thromb Vasc Biol, 2016. **36**(9): p. 1753-7.

812 32. Salmon, M., et al., *KLF4 regulates abdominal aortic aneurysm morphology and*
813 *deletion attenuates aneurysm formation*. Circulation, 2013. **128**(11 Suppl 1): p.
814 S163-74.
815 33. Pope, N.H., et al., *D-series resolvins inhibit murine abdominal aortic aneurysm*
816 *formation and increase M2 macrophage polarization*. FASEB J, 2016. **30**(12): p.
817 4192-4201.
818 34. Fashandi, A.Z., et al., *Female Mice Exhibit Abdominal Aortic Aneurysm Protection in*
819 *an Established Rupture Model*. J Surg Res, 2020. **247**: p. 387-396.
820 35. Lu, H., et al., *Subcutaneous Angiotensin II Infusion using Osmotic Pumps Induces*
821 *Aortic Aneurysms in Mice*. J Vis Exp, 2015(103).
822 36. Bhamidipati, C.M., et al., *Development of a novel murine model of aortic aneurysms*
823 *using peri-adventitial elastase*. Surgery, 2012. **152**(2): p. 238-46.
824 37. Millar, J.K., et al., *Endothelial to mesenchymal transition in the interleukin-1 pathway*
825 *during aortic aneurysm formation*. J Thorac Cardiovasc Surg, 2024. **167**(5): p. e146-
826 e158.
827 38. Doerrier, C., et al., *High-Resolution FluoRespirometry and OXPHOS Protocols for*
828 *Human Cells, Permeabilized Fibers from Small Biopsies of Muscle, and Isolated*
829 *Mitochondria*. Methods Mol Biol, 2018. **1782**: p. 31-70.
830 39. Tyrrell, D.J., et al., *Age-Associated Mitochondrial Dysfunction Accelerates*
831 *Atherogenesis*. Circ Res, 2020. **126**(3): p. 298-314.
832 40. Sidarala, V., et al., *Mitofusin 1 and 2 regulation of mitochondrial DNA content is a*
833 *critical determinant of glucose homeostasis*. Nat Commun, 2022. **13**(1): p. 2340.
834 41. Cavalli, G., et al., *Interleukin 37 reverses the metabolic cost of inflammation,*
835 *increases oxidative respiration, and improves exercise tolerance*. Proc Natl Acad Sci
836 U S A, 2017. **114**(9): p. 2313-2318.
837 42. LaRocca, T.J., et al., *Mitochondrial quality control and age-associated arterial*
838 *stiffening*. Exp Gerontol, 2014. **58**: p. 78-82.
839 43. Sun, N., et al., *Measuring In Vivo Mitophagy*. Mol Cell, 2015. **60**(4): p. 685-96.
840 44. Bravo-San Pedro, J.M., G. Kroemer, and L. Galluzzi, *Autophagy and Mitophagy in*
841 *Cardiovascular Disease*. Circ Res, 2017. **120**(11): p. 1812-1824.
842 45. Clement, M., et al., *Vascular Smooth Muscle Cell Plasticity and Autophagy in*
843 *Dissecting Aortic Aneurysms*. Arterioscler Thromb Vasc Biol, 2019. **39**(6): p. 1149-
844 1159.
845 46. Chen, J., et al., *Age-induced prostaglandin E(2) impairs mitochondrial fitness and*
846 *increases mortality to influenza infection*. Nat Commun, 2022. **13**(1): p. 6759.
847 47. Dunn, J. and M.H. Grider, *Physiology, Adenosine Triphosphate*, in *StatPearls*. 2024:
848 Treasure Island (FL).
849 48. Talley, J.T. and S.S. Mohiuddin, *Biochemistry, Fatty Acid Oxidation*, in *StatPearls*.
850 2024: Treasure Island (FL).
851 49. Castelli, S., et al., *Adaptive antioxidant response to mitochondrial fatty acid*
852 *oxidation determines the proliferative outcome of cancer cells*. Cancer Lett, 2023.
853 **554**: p. 216010.
854 50. Stine, K.J., *Application of Porous Materials to Carbohydrate Chemistry and*
855 *Glycoscience*. Adv Carbohydr Chem Biochem, 2017. **74**: p. 61-136.

856 51. Ipata, P.L. and F. Balestri, *The functional logic of cytosolic 5'-nucleotidases*. Curr
857 Med Chem, 2013. **20**(34): p. 4205-16.
858 52. Zhang, N., *Role of methionine on epigenetic modification of DNA methylation and*
859 *gene expression in animals*. Anim Nutr, 2018. **4**(1): p. 11-16.
860 53. Hasanuzzaman, M., et al., *Regulation of Ascorbate-Glutathione Pathway in*
861 *Mitigating Oxidative Damage in Plants under Abiotic Stress*. Antioxidants (Basel),
862 2019. **8**(9).
863 54. Zhang, R., et al., *Mitophagy in cardiovascular homeostasis*. Mech Ageing Dev, 2020.
864 **188**: p. 111245.
865 55. Li, A., et al., *Mitochondrial autophagy: molecular mechanisms and implications for*
866 *cardiovascular disease*. Cell Death Dis, 2022. **13**(5): p. 444.
867 56. Li, X., et al., *Inflammation and aging: signaling pathways and intervention therapies*.
868 Signal Transduct Target Ther, 2023. **8**(1): p. 239.
869 57. Esteban-Martinez, L., E. Sierra-Filardi, and P. Boya, *Mitophagy, metabolism, and cell*
870 *fate*. Mol Cell Oncol, 2017. **4**(5): p. e1353854.
871 58. Lee, J.J., et al., *Basal mitophagy is widespread in Drosophila but minimally affected*
872 *by loss of Pink1 or parkin*. J Cell Biol, 2018. **217**(5): p. 1613-1622.
873 59. Ganley, I.G., A.J. Whitworth, and T.G. McWilliams, *Comment on "mt-Keima detects*
874 *PINK1-PRKN mitophagy in vivo with greater sensitivity than mito-QC"*. Autophagy,
875 2021. **17**(12): p. 4477-4479.
876 60. Tavris, B.S., et al., *Mitochondrial Dysfunction and Increased DNA Damage in*
877 *Vascular Smooth Muscle Cells of Abdominal Aortic Aneurysm (AAA-SMC)*. Oxid Med
878 Cell Longev, 2023. **2023**: p. 6237960.
879 61. Miller, F.J., Jr., et al., *Oxidative stress in human abdominal aortic aneurysms: a*
880 *potential mediator of aneurysmal remodeling*. Arterioscler Thromb Vasc Biol, 2002.
881 **22**(4): p. 560-5.
882 62. Xia, Y., et al., *Mitochondrial Homeostasis in VSMCs as a Central Hub in Vascular*
883 *Remodeling*. Int J Mol Sci, 2023. **24**(4).
884 63. Ramadan, A., et al., *Loss of vascular smooth muscle cell autophagy exacerbates*
885 *angiotensin II-associated aortic remodeling*. J Vasc Surg, 2018. **68**(3): p. 859-871.
886 64. Zamorano-Leon, J.J., et al., *Factor Xa Inhibition by Rivaroxaban Modified*
887 *Mitochondrial-Associated Proteins in Human Abdominal Aortic Aneurysms*. Ann
888 Vasc Surg, 2020. **67**: p. 482-489.
889 65. Zhong, W., et al., *Defective mitophagy in aged macrophages promotes*
890 *mitochondrial DNA cytosolic leakage to activate STING signaling during liver sterile*
891 *inflammation*. Aging Cell, 2022. **21**(6): p. e13622.
892 66. Li, C., et al., *Impaired mitophagy causes mitochondrial DNA leakage and STING*
893 *activation in ultraviolet B-irradiated human keratinocytes HaCaT*. Arch Biochem
894 Biophys, 2023. **737**: p. 109553.
895 67. Zimmermann, M. and A.S. Reichert, *How to get rid of mitochondria: crosstalk and*
896 *regulation of multiple mitophagy pathways*. Biol Chem, 2017. **399**(1): p. 29-45.
897 68. Wang, S., et al., *The mitophagy pathway and its implications in human diseases*.
898 Signal Transduct Target Ther, 2023. **8**(1): p. 304.

69. Wei, Y., et al., *Prohibitin 2 Is an Inner Mitochondrial Membrane Mitophagy Receptor*. Cell, 2017. **168**(1-2): p. 224-238 e10.
70. Sun, S., et al., *The interaction between E3 ubiquitin ligase Parkin and mitophagy receptor PHB2 links inner mitochondrial membrane ubiquitination to efficient mitophagy*. J Biol Chem, 2022. **298**(12): p. 102704.
71. Salabei, J.K. and B.G. Hill, *Mitochondrial fission induced by platelet-derived growth factor regulates vascular smooth muscle cell bioenergetics and cell proliferation*. Redox Biol, 2013. **1**(1): p. 542-51.
72. Cardon, I., et al., *Serotonin effects on human iPSC-derived neural cell functions: from mitochondria to depression*. Mol Psychiatry, 2024.
73. Fanibunda, S.E., et al., *Serotonin regulates mitochondrial biogenesis and function in rodent cortical neurons via the 5-HT(2A) receptor and SIRT1-PGC-1alpha axis*. Proc Natl Acad Sci U S A, 2019. **116**(22): p. 11028-11037.
74. Nishimura, M., et al., *Upregulated Kynurenine Pathway Enzymes in Aortic Atherosclerotic Aneurysm: Macrophage Kynureninase Downregulates Inflammation*. J Atheroscler Thromb, 2021. **28**(11): p. 1214-1240.
75. Ramprasath, T., et al., *Tryptophan Catabolism and Inflammation: A Novel Therapeutic Target For Aortic Diseases*. Front Immunol, 2021. **12**: p. 731701.
76. Metghalchi, S., et al., *Indoleamine 2 3-dioxygenase knockout limits angiotensin II-induced aneurysm in low density lipoprotein receptor-deficient mice fed with high fat diet*. PLoS One, 2018. **13**(3): p. e0193737.
77. Fang, T.Z., et al., *Knockout or inhibition of USP30 protects dopaminergic neurons in a Parkinson's disease mouse model*. Nat Commun, 2023. **14**(1): p. 7295.
78. Liu, Y., et al., *Inhibition of USP30 Promotes Mitophagy by Regulating Ubiquitination of MFN2 by Parkin to Attenuate Early Brain Injury After SAH*. Transl Stroke Res, 2023.
79. Andrew Lee , et al., *Enhancement of mmitophagy via USP30 inhibition as a theraputic strategy for acute kidney injery*, in *ISN World Congress of Nephrology (WCN) 2024*. 2024, the International Society of Nephrology: Buenos Aires, Argentina. p. A1-A2, S1-S662.
80. Lin, C.Y., et al., *Promotion of mitochondrial biogenesis via the regulation of PARIS and PGC-1alpha by parkin as a mechanism of neuroprotection by carnosic acid*. Phytomedicine, 2021. **80**: p. 153369.

933 **Figure 1. mito-QC aged mouse aortas demonstrate decreased mitophagy in aortic VSMCs and**
934 **endothelial cells and a reduction of PINK1/Parkin expression.** (A) Aortas of young (Y, 8-10 weeks, n=5)
935 and aged (A,18-20 months, n=5) mito-QC male mice were isolated and enzymatically digested into single-
936 cell suspensions, followed by incubation with flow cytometric antibodies conjugated distinct fluorophores.
937 (B) Pseudo color plots for visualizing comparisons of Y and A mitophagy levels (Compensated area for
938 GFP vs. Compensated area for mCherry). (C) Mitophagy levels of different cellular populations between Y
939 and A aorta were quantified by calculating the ratios of mean fluorescence intensity (MFI) of mCherry
940 versus GFP. (D) Protein levels of mTOR, DRP1, PGC1α, Paris, PINK1, Parkin, Nix, PHB2 and LC3I/II in
941 the Y and A aortas were determined by Western Blot (n = 4/group) and normalized to Vinculin (E). Results
942 are presented as mean ± SEM. Unpaired two-tailed Student's t-test or Mann-Whitney U test were used for
943 statistical analysis.

944 **Figure 2. Mitophagy is also Reduced in VSMCs in Angiotensin II induced AAAs** (A) Schematic of
945 the murine AAA AngII model. Briefly, AAV containing murine PCSK9 gain-of function mutation was
946 administrated through a single intraperitoneal injection in conjunction with 42% HFD for 6 weeks. After
947 2-weeks HFD, the mice were subjected to subcutaneous implantation of an Ang II pump delivering a
948 dosage of 1000ng/kg/min for 4 weeks. Subsequently, aortas from three experimental groups – chow diet
949 with a saline pump, HFD with a saline pump and HFD with an AngII pump (8-12 weeks, n=5 per group,
950 mito-QC mice) – were harvested, digested into single-cell suspensions, and then subjected to the same
951 flow cytometric antibodies as described in Figure 1. (B) Mitophagy levels of endothelial cells ($CD45^-$
952 $CD31^+$), $CD45^+$ cellular population, α-$actin^{high}$ VSMCs (CD31-CD45-α-$actin^{high}$) and α-$actin^{low}$ VSMCs
953 (CD31-CD45-α-$actin^{low}$) were quantified by calculating the ratios of mean fluorescence intensity (MFI) of
954 mCherry versus GFP. (C) Pseudo color plots for visualizing comparisons of three groups' mitophagy
955 levels (Compensated area for GFP vs. Compensated area for mCherry). (D) Representative images of
956 frozen-sectioned slides from three groups mentioned above, displaying the GFP and mCherry
957 fluorescence within the aortic tissue. The mCherry puncta represents mito-lysosomes. The quantification
958 of the percentage of mito-lysosomes within ROI is shown in (E). (F) IF staining of α-actin, LAMP-1 and
959 TOMM20 of aortic slides from HFD + Saline or AngII pump group. Results are presented by mean ±
960 SEM. Unpaired two-tailed Student's t-test or Mann-Whitney U test were used for statistical analysis.

961 **Figure 3. Parkin expression is diminished within the AAA tissue, concomitant with a reduction in the**
962 **content of mitochondrial complexes.** (A) mRNA levels of mitophagy related genes in the aortic tissue of
963 HFD with saline pump (HS) and AAA groups (n=5 per group), including Park2, ACTA2, MYH11, ATG5,
964 MAP1LC3b and PINK1, with r18s as housekeeping gene. (B-C) Protein levels in the aortic tissue of HS
965 and AAA groups, including PGC1α, TBK1, PINK1, Parkin, α-actin, STING, Nix, PHB2 and LC3II were
966 determined by Western blot (n=4 per group), employing GAPDH as internal control for quantification. (D-
967 E) Representative aortic IHC staining images and quantification of Parkin and PINK1 in the HS and AAA
968 group (n=5 per group). (F-G) The contents of four representative proteins associated with mitochondrial
969 complexes within the aortic tissues in HS and AAA group, including complex V - ATP5A, complex III -
970 UQCRC2, complex II - SDHB, complex I - NDUFB8, were determined by Western blot, utilizing VDAC1
971 as internal control for quantification. Results are presented by mean ± SEM. Unpaired two-tailed Student's
972 t-test or Mann-Whitney U test were used for statistical analysis.

973

Figure 4. Mitophagy mediators PINK1 and Parkin exhibited a decreasing trend in both gene and protein expression levels in human AAA tissues. (A) Gene expression analysis of mitophagy-related genes (including PARK2, PINK1, BNIP3, BNIP3L, USP30, PHB2, ATG5, ATG7, MAPLC3B, AMBRA1, BECN1, FUNDC1, OPTN, and PPARGC1A) was conducted on human control (n=44) and AAA (n=96) tissues using bulk RNA sequencing. (B-C) Protein levels of PGC1α, PINK1, Parkin, Sting, Nix, and LC3I/II were assessed in human aortic tissue from healthy aorta and AAA groups (n=5-7 per group) by Western blot, with GAPDH used as an internal control for quantification. Results are presented as mean ± SEM. Statistical analysis was performed using an unpaired two-tailed Student's t-test or Mann-Whitney U test.

Figure 5. Parkin deficiency in the VSMCs is associated with an increased propensity for AAA rupture and augmented maximal aortic diameter, concomitant with enhanced mitochondrial dysfunction. (A) Schematic of AngII AAA model in Myh11-creERT2 Parkin fl/fl mice cohort. Tamoxifen was administered via intraperitoneal injection at a daily dosage of 75mg/kg for 5 days. After a 9-days interval, the standard procedure for AAA was implemented. (B) Kaplan-Meier survival curves, AAA incidence rate, and maximal aneurysmal diameters in control (n=35) versus Parkin SMCKO (n=39) groups. Log rank test was used for survival analysis. Fisher's exact test was used for incidence analysis. (C) Representative images of dissected aortas were presented from control and Parkin SMCKO groups. (D) IF staining of α-actin, LAMP-1 and TOMM20 on aortic slides from control vs. Parkin SMCKO group. (E-F) Protein levels in the aneurysms of control and Parkin SMCKO groups, including PINK1, STING, Nix, PHB2, LC3II/I and GAPDH, were determined by Western blot (n=4 per group), employing GAPDH as internal control for quantification. (G) Representative images of frozen-sectioned AAA slides stained with MitoSoxred from control vs. Parkin SMCKO groups are displayed. (H) mtDNA copy numbers in the AAAs of control vs Parkin SMCKO groups were determined by evaluating the fold change ratios of mt9/mt11 versus Ndufv1 respectively, a gene in mtDNA and nuclear DNA encoding the proteins for mitochondrial complex I. (I-J) The contents of four representative proteins associated with mitochondrial complexes within the aortic tissues in control and Parkin SMCKO group, including complex V - ATP5A, complex III - UQCRC2, complex II - SDHB, complex I - NDUFB8, were determined by Western blot, utilizing VDAC1 as internal control for quantification. (K) Representative protocol for measuring the maximal oxygen consumption rate (OCR) using substrates, inhibitors and uncoupler (see methods). (L) Maximal aortic OCR with substrates for complex I and I+II coupled oxidative phosphorylation (OXPHOS) and maximal OCR for complex I+II and complex II in uncoupled conditions, using the AAA tissues from control and Parkin SMCKO groups. 2-way ANOVA with Sidak's multiple comparison test were used for **L**. Results are presented by mean ± SEM. Unpaired two-tailed Student's t-test or Mann-Whitney U test were used for statistical analysis for **B (3)**, **I**, **F** and **J**. Results are presented by mean ± SEM. Unpaired two-tailed Student's t-test or Mann-Whitney U test were used for statistical analysis for **B (3)**, **I**, **F** and **J**.

Figure 6. Serum metabolomics data showed mitochondrial dysfunction in Parkin SMCKO AAA mice. Metabolomic analysis was performed on serum samples from ctrl and Parkin SMCKO group (n=5 per group). PLS-DA analysis was performed after normalization of the values (A). The heat map was plotted by top 50 metabolites from two groups (B). The Volcano map was plotted with the threshold as p-value≤0.05 and Log2FC≥ ± 1.5 (C). VIP plot showed the scores of VIP features in different metabolomic pathways that discriminate between Control and Parkin SMCKO group (D).

1018 **Figure 7. Angiotensin II reduces mitophagy levels of VSMCs, leading to increased mtROS and**
1019 **mitochondria dysfunction, while USP30 inhibition via VB-08 ameliorates the outcome in vitro.** (A)
1020 Pseudocolor plots for visualizing the mitophagy levels by gating the cells with lower MFI ratio of GFP
1021 versus mCherry. Cells are primary VSMCs isolated from Mito-QC mice, treated with 100nM, 500nM and
1022 1000nM AngII (n=3 per group). (B) The MFI of MitoSox Red in MOVAS treated with 100nM, 500nM,
1023 and 1000nM AngII (n=6 per group). (C-E) The MFI of Mtphagy dye (n=7 per group) and MitoSox Red
1024 (n=6 per group) within MOVAS respectively treated with vehicle, 100nM AngII, or a combination of
1025 100nM AngII with 100nM VB-08, were quantified and showed in a histogram, same for the MFI of
1026 Mitotracker and TMRM. The MFI ratio of TMRM to Mitotracker was employed as a metric for assessing
1027 the proportion of healthy mitochondria within the cells. (F-G) Alteration of protein levels in MOVAS after
1028 treatment with AngII alone or AngII in combination with VB-08, including PGC1α, Parkin, LC3I/II, were
1029 determined by Western blot (n=4 per group). β-tubulin is the internal control for normalization. (H) For
1030 MOVAS transfected with lentiviral scrambled or Parkin shRNA, the MFI of MitoSox Red within cells
1031 treated with vehicle, 100nM AngII, or a combination of 100nM AngII with 100nM VB-08 (n=12 per group),
1032 were quantified, same for the MFI ratio of TMRM to Mitotracker. Results are presented as mean ± SEM.
1033 Unpaired two-tailed Student's t-test or Mann-Whitney U test were used for statistical analysis. Two-way
1034 ANOVA was used for **H**.

1035 **Figure 8. VB-08, a USP30 inhibitor, reduces aneurysm incidence and maximal aortic diameters in**
1036 **vivo during Ang II infusion.** (A) The strategy for inducing and therapeutically targeting AAA with VB-
1037 08 in C57BL/6 male mice cohort. (B) Kaplan-Meier survival curve, AAA incidence rate, and maximal
1038 diameters of aneurysms in blank (n=23), vehicle (n=25), and VB-08 (n=25) groups. Log rank test was
1039 used for survival analysis. Fisher's exact test was used for incidence rate analysis. (C) The representative
1040 images of dissected aortas in the vehicle vs. VB-08 group. (D-E) Protein levels in the descending aortas
1041 of vehicle vs. VB-08 inhibitor groups, including PGC1α, PINK1, Parkin, STING, Nix, PHB2, LC3II/I
1042 and GAPDH, were determined by Western blot (n=5 per group), employing GAPDH as internal control
1043 for quantification. (F) mtDNA copy numbers in the aorta of vehicle vs. VB-08 treated group were
1044 determined by evaluating the fold change ratios of mt9/mt11 versus Ndufv1. (G) Maximal aortic OCR
1045 with substrates for complex I and I+II coupled oxidative phosphorylation (OXPHOS) and maximal OCR
1046 for complex I+II and complex II in uncoupled conditions, using the aortic tissues from vehicle vs. VB-08
1047 groups (n = 8-9 per group).

1048

1049 **Figure 9. Serum metabolomics data showed altered metabolites in AAA mice following USP30**
1050 **inhibition by VB-08.** Metabolomic analysis was performed on serum samples from vehicle and VB-08
1051 group (n=7 per group) in AAA mice. PLS-DA analysis was performed after normalization of the values
1052 (A). The Volcano map was plotted with the threshold as p-value≤0.05 and Log2FC≥ ± 1.5 (B). The heat
1053 map was plotted by top 50 metabolites from two groups (C). VIP plot showed the scores of VIP features
1054 in different metabolomic pathways that discriminate between vehicle and VB-08 group (D).

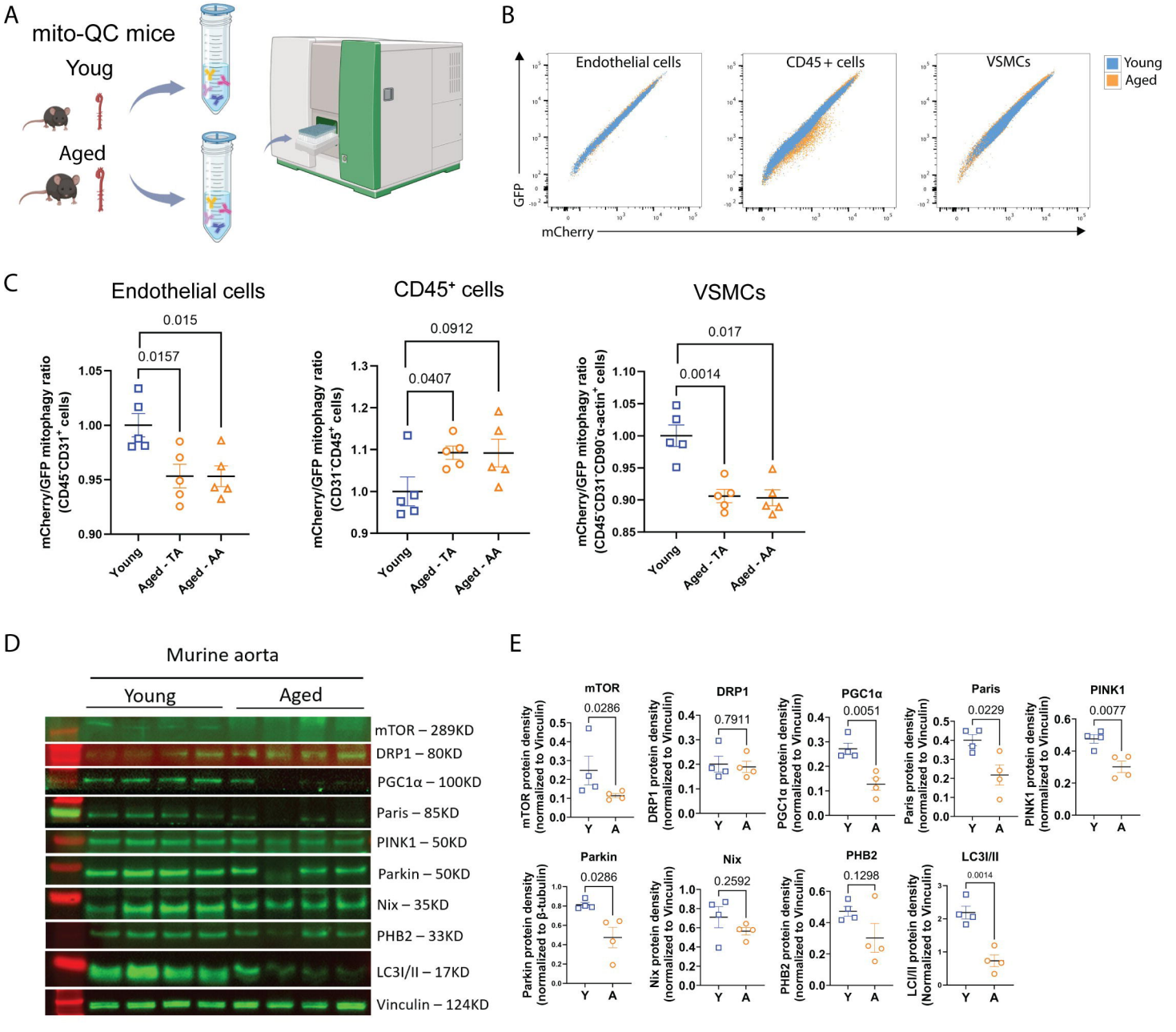
A
mito-QC mice
Youg
Aged
B
Endothelial cells
CD45 + cells
VSMCs
Young
Aged
GFP
mCherry
C
Endothelial cells
CD45⁺ cells
VSMCs
mCherry/GFP mitophagy ratio (CD45⁻CD31⁺ cells)
mCherry/GFP mitophagy ratio (CD31⁻CD45⁺ cells)
mCherry/GFP mitophagy ratio (CD45⁻CD31⁻CD90⁻α-actin⁺ cells)
0.015
0.0157
0.0912
0.0407
0.017
0.0014
Young
Aged - TA
Aged - AA
D
Murine aorta
Young
Aged
mTOR – 289KD
DRP1 – 80KD
PGC1α – 100KD
Paris – 85KD
PINK1 – 50KD
Parkin – 50KD
Nix – 35KD
PHB2 – 33KD
LC3I/II – 17KD
Vinculin – 124KD
E
mTOR
DRP1
PGC1α
Paris
PINK1
Parkin
Nix
PHB2
LC3I/II
mTOR protein density (normalized to Vinculin)
DRP1 protein density (normalized to Vinculin)
PGC1α protein density (normalized to Vinculin)
Paris protein density (normalized to Vinculin)
PINK1 protein density (normalized to Vinculin)
Parkin protein density (normalized to β-tubulin)
Nix protein density (normalized to Vinculin)
PHB2 protein density (normalized to Vinculin)
LCI/II protein density (Normalized to Vinculin)
0.0286
0.7911
0.0051
0.0229
0.0077
0.0286
0.2592
0.1298
0.0014
Y
A

A

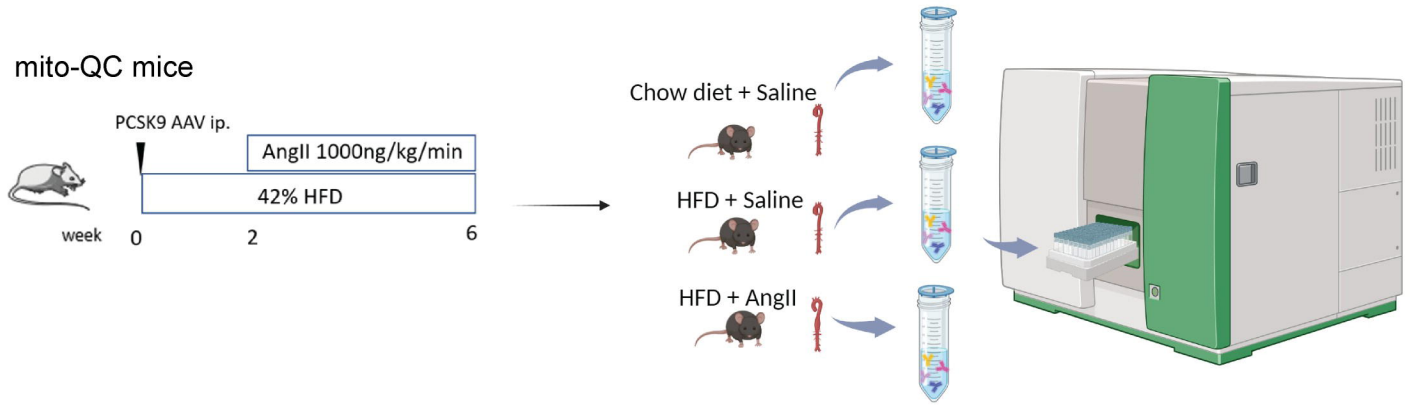
mito-QC mice
PCSK9 AAV ip.
AngII 1000ng/kg/min
42% HFD
week
0
2
6
Chow diet + Saline
HFD + Saline
HFD + AngII

B

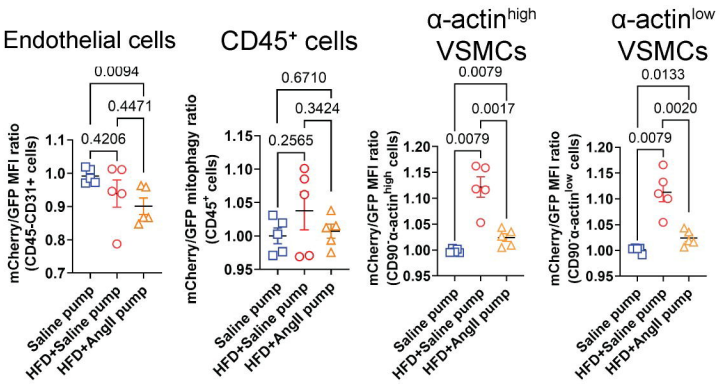
Endothelial cells
CD45⁺ cells
α-actin^high VSMCs
α-actin^low VSMCs
mCherry/GFP MFI ratio (CD45-CD31+ cells)
mCherry/GFP mitophagy ratio (CD45⁺ cells)
mCherry/GFP MFI ratio (CD90⁻α-actin^high cells)
mCherry/GFP MFI ratio (CD90⁻α-actin^low cells)
0.0094
0.4471
0.4206
0.6710
0.3424
0.2565
0.0079
0.0017
0.0079
0.0133
0.0020
0.0079
Saline pump
HFD+Saline pump
HFD+AngII pump

C

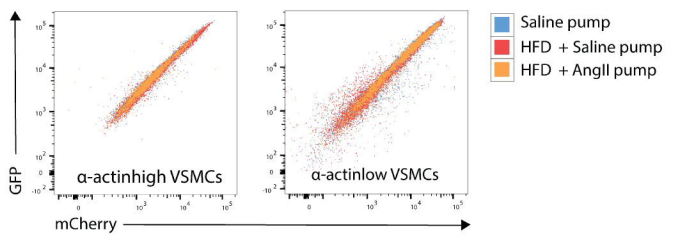
GFP
mCherry
α-actinhigh VSMCs
α-actinlow VSMCs
Saline pump
HFD + Saline pump
HFD + AngII pump

C

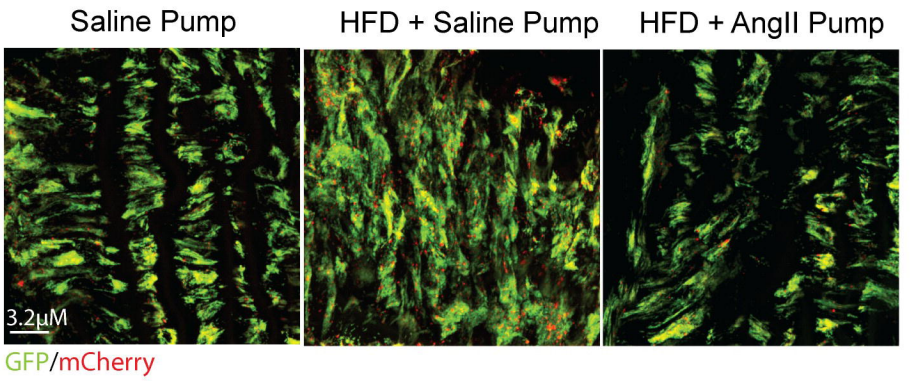
Saline Pump
HFD + Saline Pump
HFD + AngII Pump
3.2μM
GFP/mCherry

D

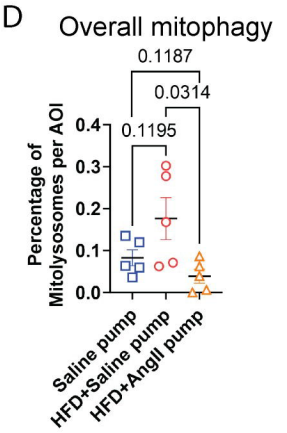
Overall mitophagy
Percentage of Mitolysosomes per AOI
0.1187
0.0314
0.1195
Saline pump
HFD+Saline pump
HFD+AngII pump

E

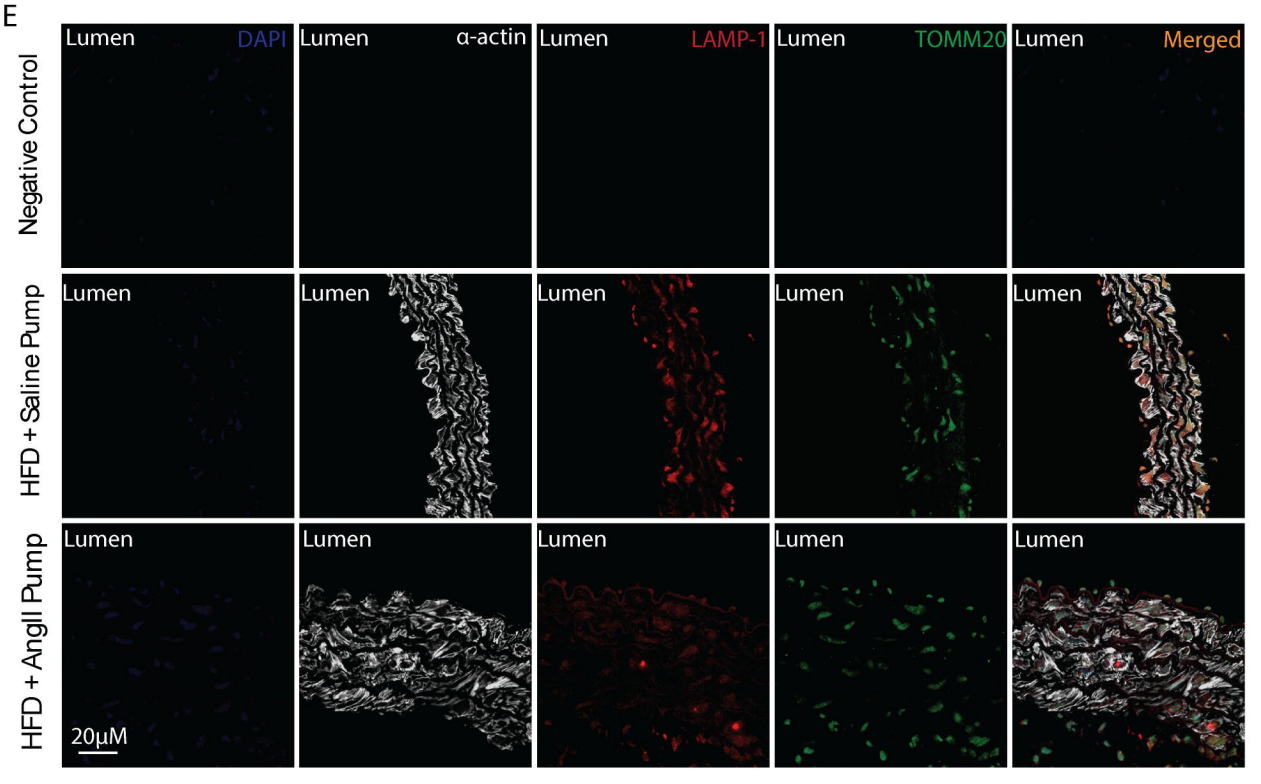
Negative Control
HFD + Saline Pump
HFD + AngII Pump
Lumen
DAPI
α-actin
LAMP-1
TOMM20
Merged
20μM

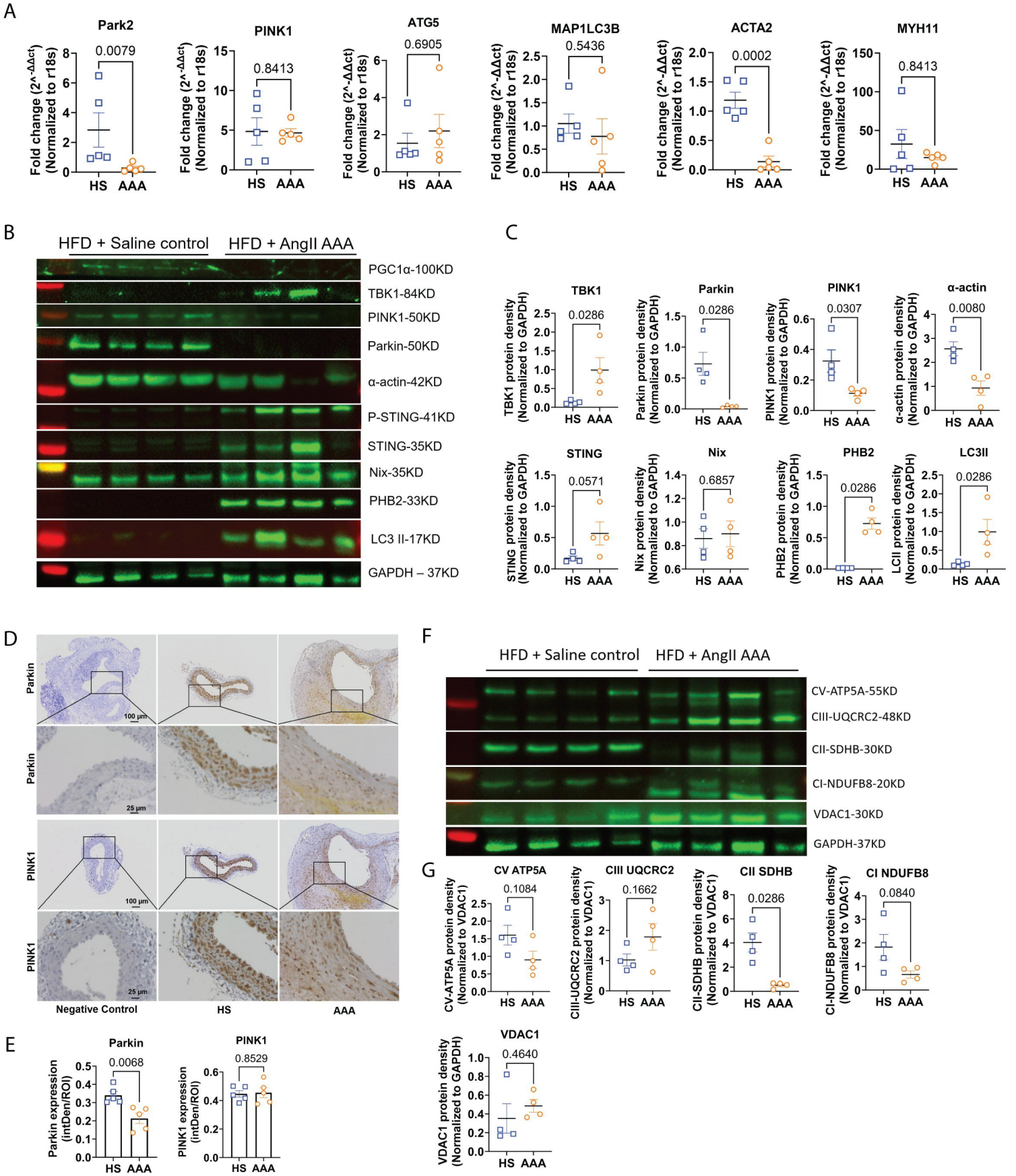
A
Park2
0.0079
PINK1
0.8413
ATG5
0.6905
MAP1LC3B
0.5436
ACTA2
0.0002
MYH11
0.8413
Fold change (2^-ΔΔct) (Normalized to r18s)
HS
AAA
B
HFD + Saline control
HFD + AngII AAA
PGC1α-100KD
TBK1-84KD
PINK1-50KD
Parkin-50KD
α-actin-42KD
P-STING-41KD
STING-35KD
Nix-35KD
PHB2-33KD
LC3 II-17KD
GAPDH – 37KD
C
TBK1
0.0286
Parkin
0.0286
PINK1
0.0307
α-actin
0.0080
STING
0.0571
Nix
0.6857
PHB2
0.0286
LC3II
0.0286
TBK1 protein density (Normalized to GAPDH)
Parkin protein density (Normalized to GAPDH)
PINK1 protein density (Normalized to GAPDH)
α-actin protein density (Normalized to GAPDH)
STING protein density (Normalized to GAPDH)
Nix protein density (Normalized to GAPDH)
PHB2 protein density (Normalized to GAPDH)
LCII protein density (Normalized to GAPDH)
D
Parkin
PINK1
100 μm
25 μm
Negative Control
HS
AAA
E
Parkin
0.0068
PINK1
0.8529
Parkin expression (intDen/ROI)
PINK1 expression (intDen/ROI)
F
HFD + Saline control
HFD + AngII AAA
CV-ATP5A-55KD
CIII-UQCRC2-48KD
CII-SDHB-30KD
CI-NDUFB8-20KD
VDAC1-30KD
GAPDH-37KD
G
CV ATP5A
0.1084
CIII UQCRC2
0.1662
CII SDHB
0.0286
CI NDUFB8
0.0840
VDAC1
0.4640
CV-ATP5A protein density (Normalized to VDAC1)
CIII-UQCRC2 protein density (Normalized to VDAC1)
CII-SDHB protein density (Normalized to VDAC1)
CI-NDUFB8 protein density (Normalized to VDAC1)
VDAC1 protein density (Normalized to GAPDH)

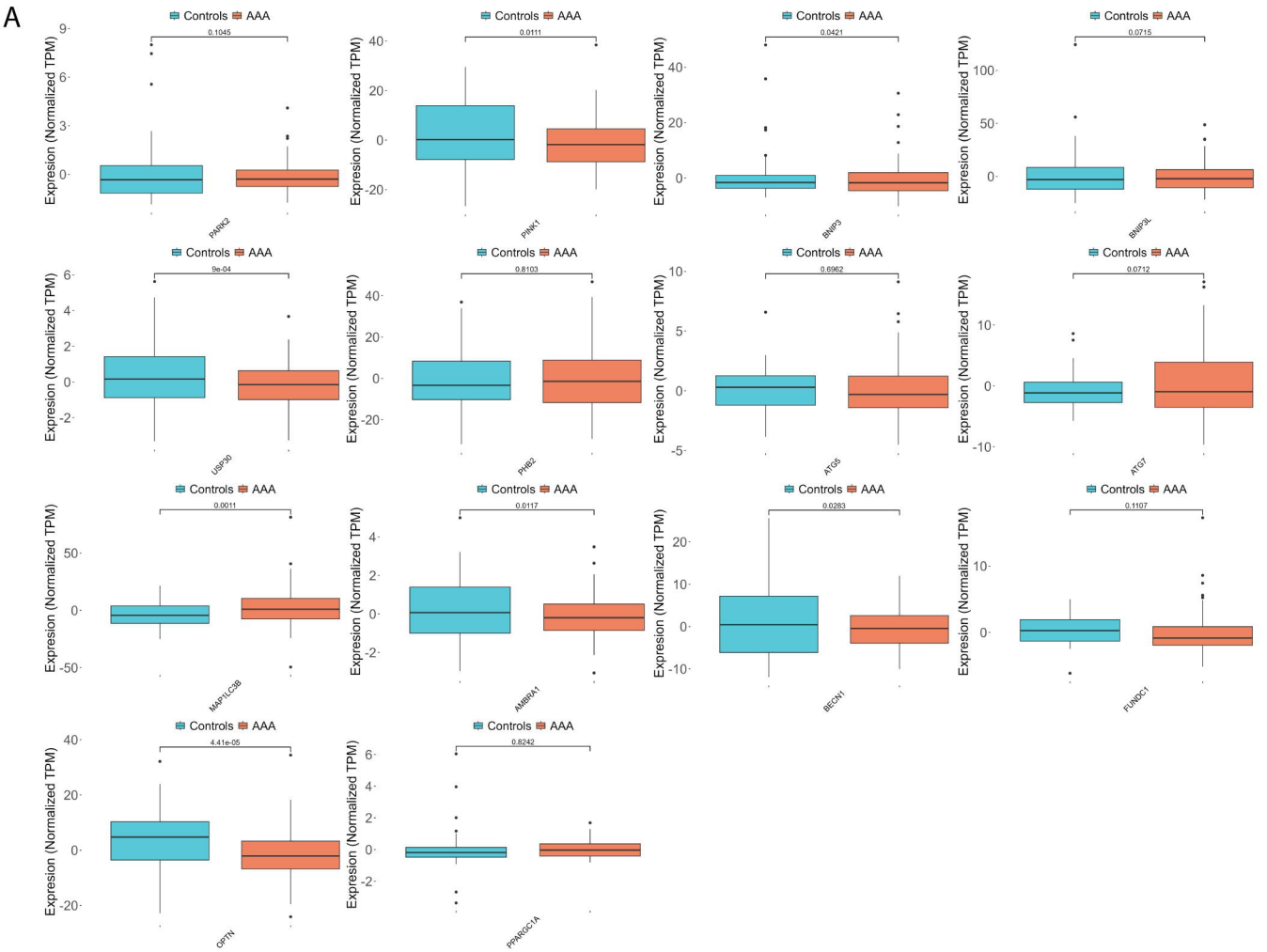
A
Controls AAA
Expresion (Normalized TPM)
0.1045
PARK2
0.0111
PINK1
0.0421
BNIP3
0.0715
BNIP3L
9e-04
USP30
0.8103
PHB2
0.6962
ATG5
0.0712
ATG7
0.0011
MAP1LC3B
0.0117
AMBRA1
0.0283
BECN1
0.1107
FUNDC1
4.41e-05
OPTN
0.8242
PPARGC1A

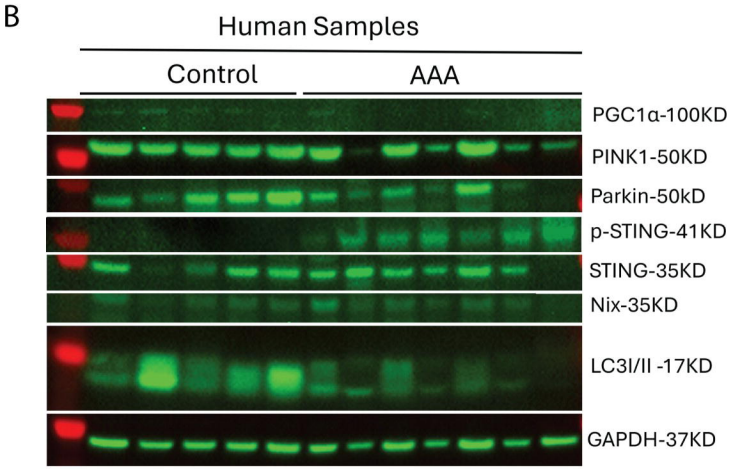
B
Human Samples
Control
AAA
PGC1α-100KD
PINK1-50KD
Parkin-50kD
p-STING-41KD
STING-35KD
Nix-35KD
LC3I/II -17KD
GAPDH-37KD

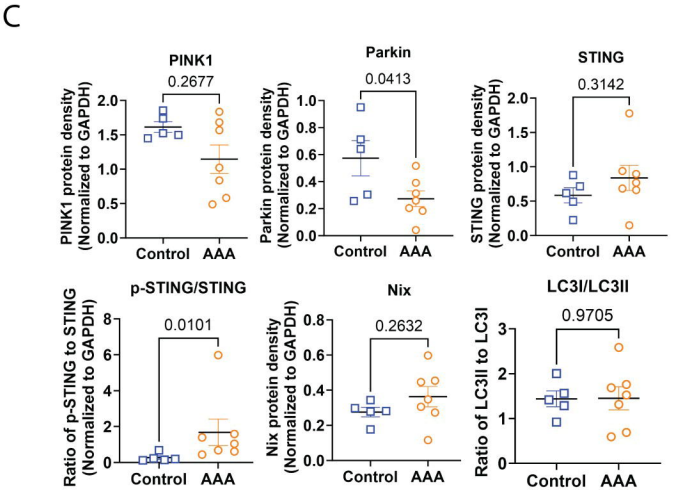
C
PINK1
0.2677
PINK1 protein density (Normalized to GAPDH)
Parkin
0.0413
Parkin protein density (Normalized to GAPDH)
STING
0.3142
STING protein density (Normalized to GAPDH)
p-STING/STING
0.0101
Ratio of p-STING to STING (Normalized to GAPDH)
Nix
0.2632
Nix protein density (Normalized to GAPDH)
LC3I/LC3II
0.9705
Ratio of LC3II to LC3I
Control
AAA

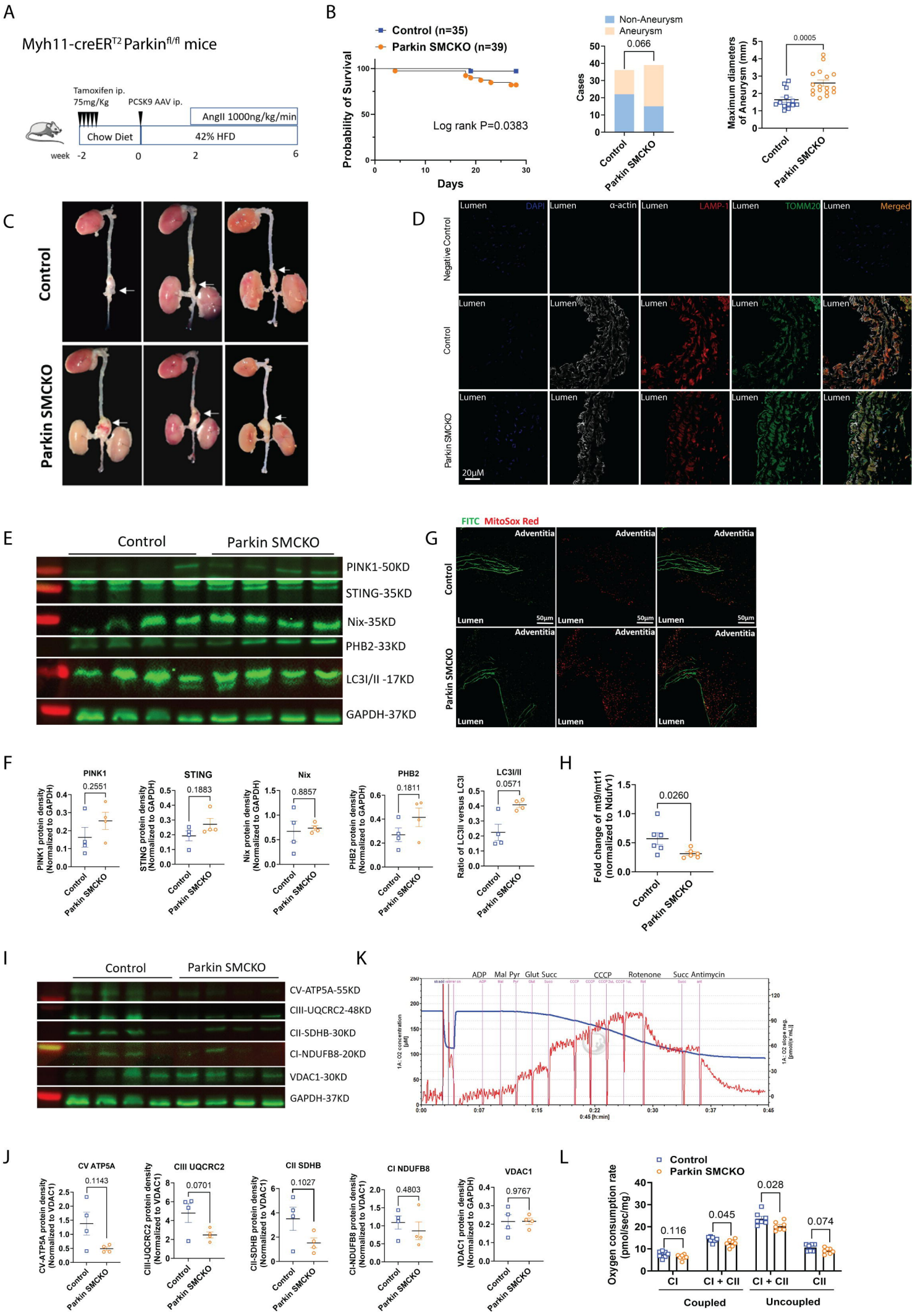
A
Myh11-creER^{T2} Parkin$^{fl/fl}$ mice
Tamoxifen ip.
75mg/Kg
PCSK9 AAV ip.
AngII 1000ng/kg/min
Chow Diet
42% HFD
week -2 0 2 6
B
Control (n=35)
Parkin SMCKO (n=39)
Probability of Survival
Log rank P=0.0383
Days
Non-Aneurysm
Aneurysm
0.066
Cases
Control
Parkin SMCKO
0.0005
Maximum diameters of Aneurysm (mm)
C
Control
Parkin SMCKO
D
Negative Control
Control
Parkin SMCKO
Lumen
DAPI
α-actin
LAMP-1
TOMM20
Merged
20μM
E
Control
Parkin SMCKO
PINK1-50KD
STING-35KD
Nix-35KD
PHB2-33KD
LC3I/II -17KD
GAPDH-37KD
G
FITC MitoSox Red
Adventitia
Lumen
50μm
F
PINK1
0.2551
PINK1 protein density (Normalized to GAPDH)
STING
0.1883
STING protein density (Normalized to GAPDH)
Nix
0.8857
Nix protein density (Normalized to GAPDH)
PHB2
0.1811
PHB2 protein density (Normalized to GAPDH)
LC3I/II
0.0571
Ratio of LC3II versus LC3I
H
0.0260
Fold change of mt9/mt11 (normalized to Ndufv1)
I
CV-ATP5A-55KD
CIII-UQCRC2-48KD
CII-SDHB-30KD
CI-NDUFB8-20KD
VDAC1-30KD
GAPDH-37KD
K
ADP Mal Pyr Glut Succ CCCP Rotenone Succ Antimycin
0:45 [h:min]
J
CV ATP5A
0.1143
CV-ATP5A protein density (Normalized to VDAC1)
CIII UQCRC2
0.0701
CIII-UQCRC2 protein density (Normalized to VDAC1)
CII SDHB
0.1027
CII-SDHB protein density (Normalized to VDAC1)
CI NDUFB8
0.4803
CI-NDUFB8 protein density (Normalized to VDAC1)
VDAC1
0.9767
VDAC1 protein density (Normalized to GAPDH)
L
Control
Parkin SMCKO
Oxygen consumption rate (pmol/sec/mg)
0.116
0.045
0.028
0.074
CI
CI + CII
CI + CII
CII
Coupled
Uncoupled

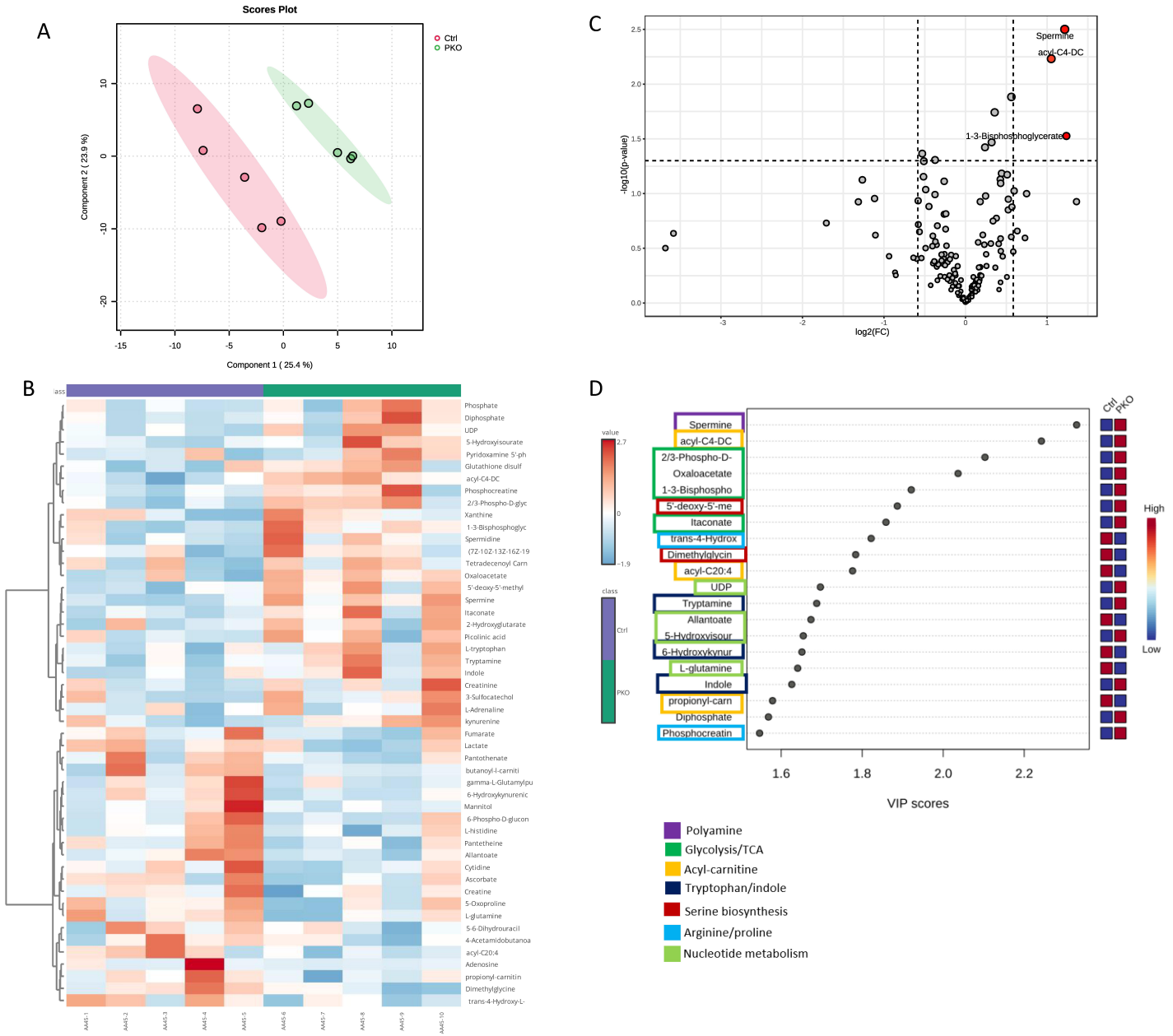
A
Scores Plot
Ctrl
PKO
Component 2 (23.9 %)
Component 1 (25.4 %)
B
class
Phosphate
Diphosphate
UDP
5-Hydroxyisourate
Pyridoxamine 5'-ph
Glutathione disulf
acyl-C4-DC
Phosphocreatine
2/3-Phospho-D-glyc
Xanthine
1-3-Bisphosphoglyc
Spermidine
(7Z-10Z-13Z-16Z-19
Tetradecenoyl Carn
Oxaloacetate
5'-deoxy-5'-methyl
Spermine
Itaconate
2-Hydroxyglutarate
Picolinic acid
L-tryptophan
Tryptamine
Indole
Creatinine
3-Sulfocatechol
L-Adrenaline
kynurenine
Fumarate
Lactate
Pantothenate
butanoyl-l-carniti
gamma-L-Glutamylpu
6-Hydroxykynurenic
Mannitol
6-Phospho-D-glucon
L-histidine
Pantetheine
Allantoate
Cytidine
Ascorbate
Creatine
5-Oxoproline
L-glutamine
5-6-Dihydrouracil
4-Acetamidobutanoa
acyl-C20:4
Adenosine
propionyl-carnitin
Dimethylglycine
trans-4-Hydroxy-L-
AA45-1
AA45-2
AA45-3
AA45-4
AA45-5
AA45-6
AA45-7
AA45-8
AA45-9
AA45-10
C
Spermine
acyl-C4-DC
1-3-Bisphosphoglycerate
-log10(p-value)
log2(FC)
D
value
2.7
0
−1.9
class
Ctrl
PKO
Spermine
acyl-C4-DC
2/3-Phospho-D-
Oxaloacetate
1-3-Bisphospho
5'-deoxy-5'-me
Itaconate
trans-4-Hydrox
Dimethylglycin
acyl-C20:4
UDP
Tryptamine
Allantoate
5-Hydroxyisour
6-Hydroxykynur
L-glutamine
Indole
propionyl-carn
Diphosphate
Phosphocreatin
Ctrl
PKO
High
Low
VIP scores
Polyamine
Glycolysis/TCA
Acyl-carnitine
Tryptophan/indole
Serine biosynthesis
Arginine/proline
Nucleotide metabolism

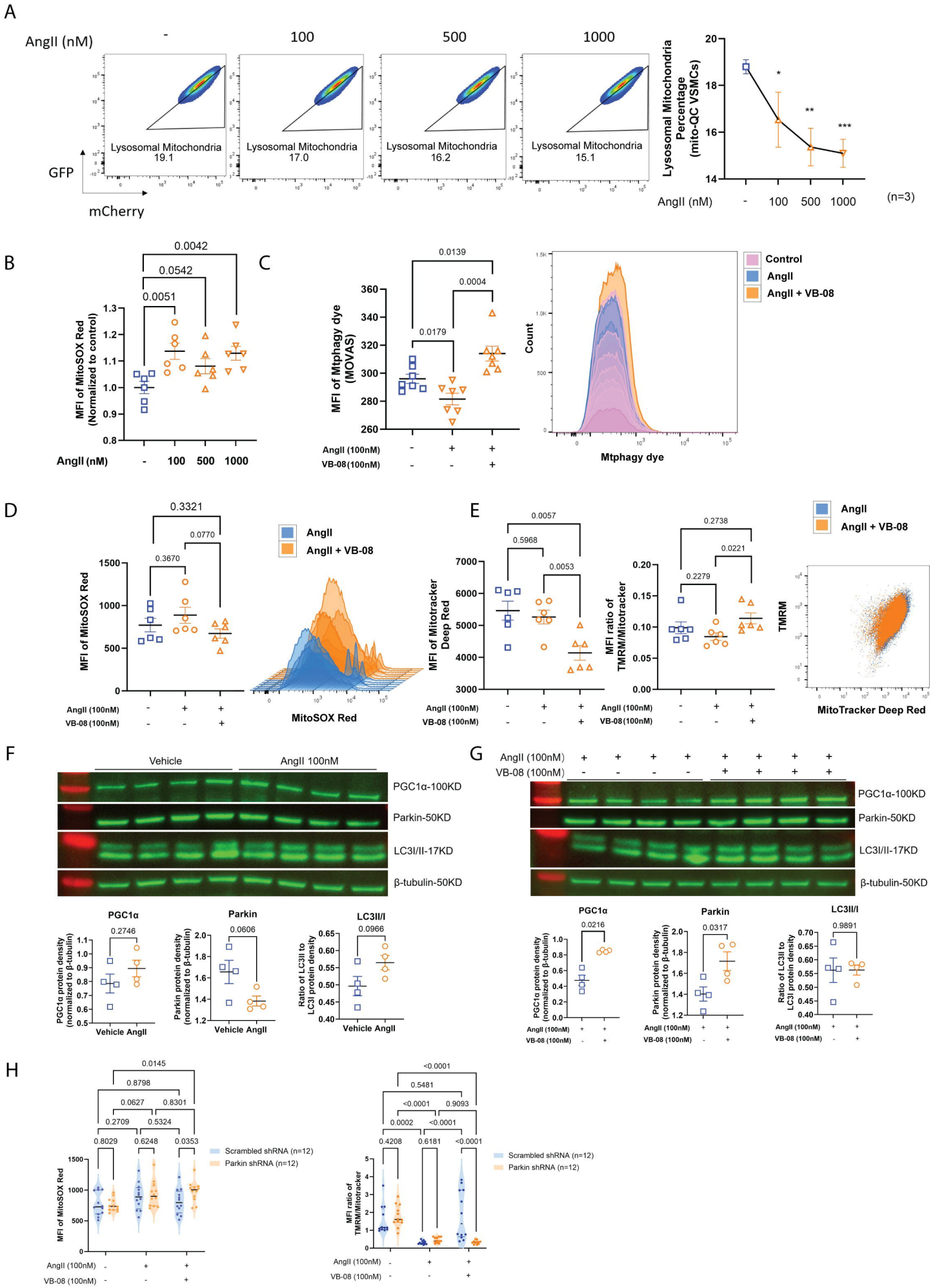
A
AngII (nM)
-
100
500
1000
Lysosomal Mitochondria 19.1
Lysosomal Mitochondria 17.0
Lysosomal Mitochondria 16.2
Lysosomal Mitochondria 15.1
GFP
mCherry
Lysosomal Mitochondria Percentage (mito-QC VSMCs)
(n=3)
B
MFI of MitoSOX Red (Normalized to control)
0.0042
0.0542
0.0051
C
MFI of Mtphagy dye (MOVAS)
0.0139
0.0004
0.0179
Count
Mtphagy dye
Control
AngII
AngII + VB-08
AngII (100nM)
VB-08 (100nM)
D
MFI of MitoSOX Red
0.3321
0.0770
0.3670
MitoSOX Red
E
MFI of Mitotracker Deep Red
0.0057
0.5968
0.0053
MFI ratio of TMRM/Mitotracker
0.2738
0.0221
0.2279
TMRM
MitoTracker Deep Red
F
Vehicle
AngII 100nM
PGC1α-100KD
Parkin-50KD
LC3I/II-17KD
β-tubulin-50KD
PGC1α
0.2746
Parkin
0.0606
LC3II/I
0.0966
PGC1α protein density (normalized to β-tubulin)
Parkin protein density (normalized to β-tubulin)
Ratio of LC3II to LC3I protein density
Vehicle AngII
G
AngII (100nM)
VB-08 (100nM)
PGC1α-100KD
Parkin-50KD
LC3I/II-17KD
β-tubulin-50KD
PGC1α
0.0216
Parkin
0.0317
LC3II/I
0.9891
H
0.0145
0.8798
0.0627
0.8301
0.2709
0.5324
0.8029
0.6248
0.0353
Scrambled shRNA (n=12)
Parkin shRNA (n=12)
MFI of MitoSOX Red
<0.0001
0.5481
<0.0001
0.9093
0.0002
<0.0001
0.4208
0.6181
<0.0001
MFI ratio of TMRM/Mitotracker

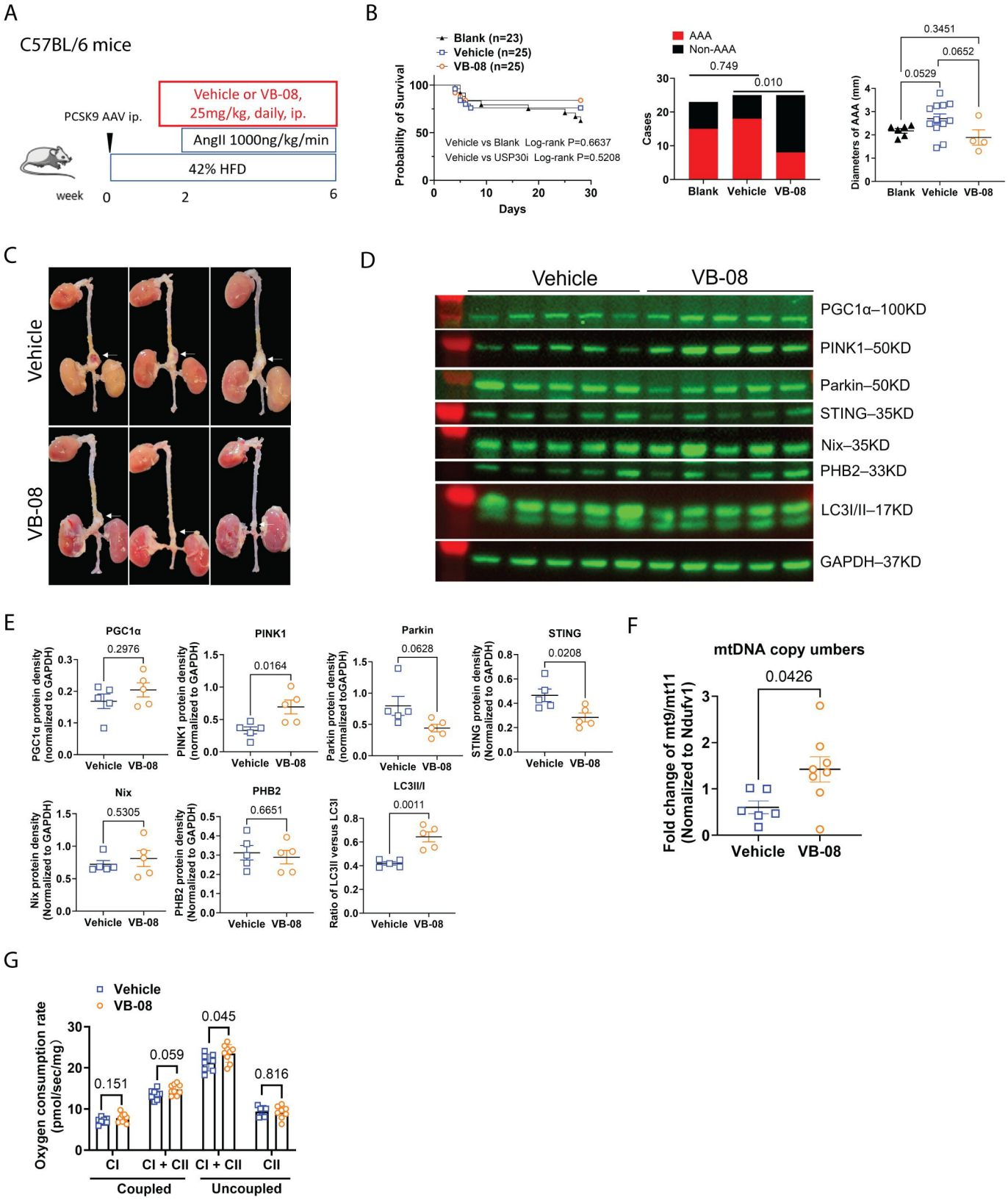
A
C57BL/6 mice
PCSK9 AAV ip.
Vehicle or VB-08, 25mg/kg, daily, ip.
AngII 1000ng/kg/min
42% HFD
week
0
2
6
B
Blank (n=23)
Vehicle (n=25)
VB-08 (n=25)
Probability of Survival
Vehicle vs Blank Log-rank P=0.6637
Vehicle vs USP30i Log-rank P=0.5208
Days
AAA
Non-AAA
0.749
0.010
Cases
Blank
Vehicle
VB-08
0.3451
0.0652
0.0529
Diameters of AAA (mm)
C
Vehicle
VB-08
D
Vehicle
VB-08
PGC1α–100KD
PINK1–50KD
Parkin–50KD
STING–35KD
Nix–35KD
PHB2–33KD
LC3I/II–17KD
GAPDH–37KD
E
PGC1α
0.2976
PGC1α protein density (normalized to GAPDH)
PINK1
0.0164
PINK1 protein density (normalized to GAPDH)
Parkin
0.0628
Parkin protein density (normalized toGAPDH)
STING
0.0208
STING protein density (Normalized to GAPDH)
Nix
0.5305
Nix protein density (Normalized to GAPDH)
PHB2
0.6651
PHB2 protein density (Normalized to GAPDH)
LC3II/I
0.0011
Ratio of LC3II versus LC3I
Vehicle
VB-08
F
mtDNA copy umbers
0.0426
Fold change of mt9/mt11 (Nomalized to Ndufv1)
Vehicle
VB-08
G
Vehicle
VB-08
Oxygen consumption rate (pmol/sec/mg)
0.151
0.059
0.045
0.816
CI
CI + CII
CI + CII
CII
Coupled
Uncoupled

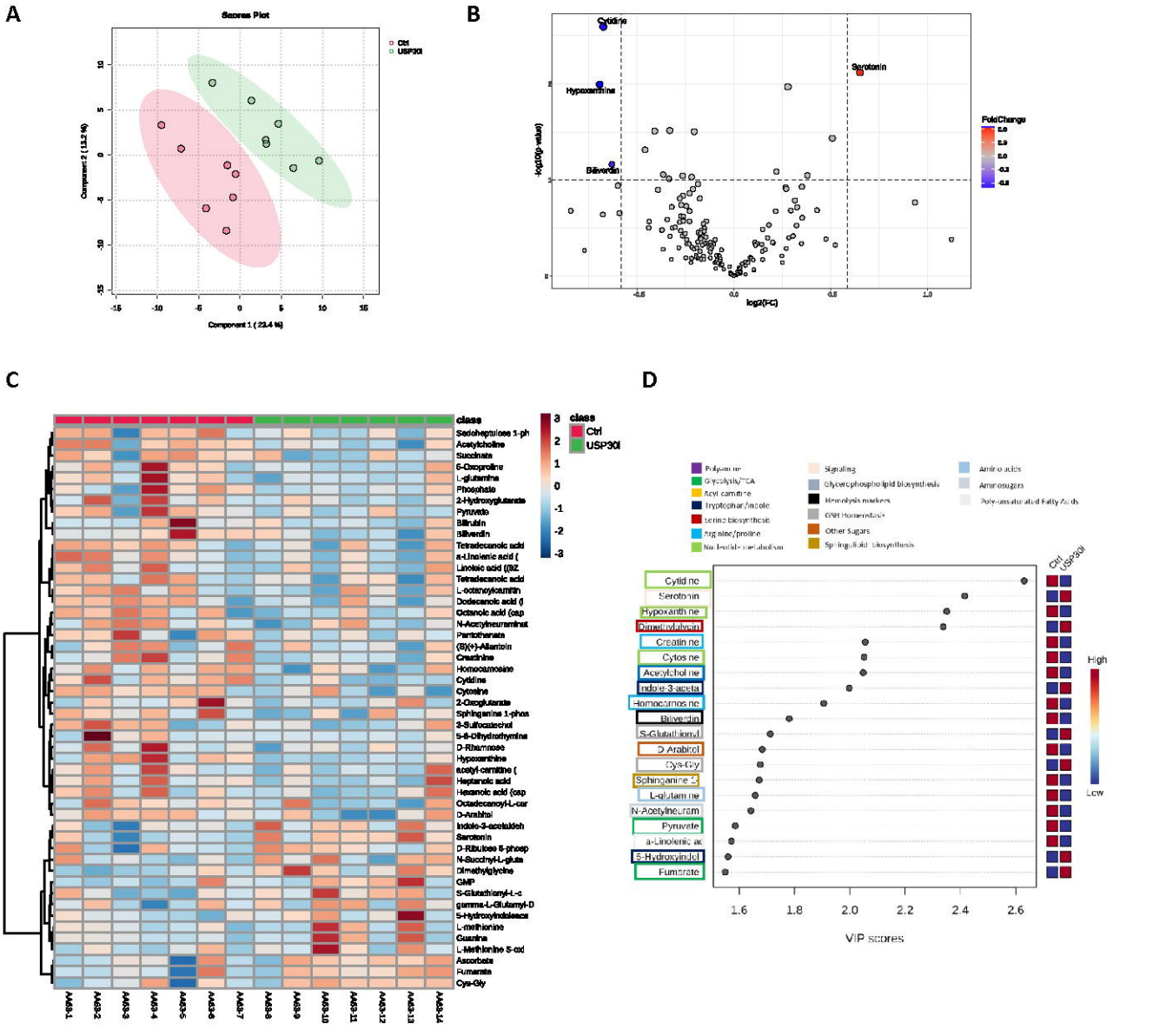
A
Scores Plot
Ctrl
USP30I
Component 1 (23.4 %)
Component 2 (13.2 %)
B
Cytidine
Serotonin
Hypoxanthine
Biliverdin
-log10(p-value)
log2(f-C)
FoldChange
C
class
Ctrl
USP30I
Sedoheptulose 1-ph
Acetylcholine
Succinate
6-Oxopurine
L-glutamine
Phosphate
2-Hydroxyglutarate
Pyruvate
Bilirubin
Biliverdin
Tetradecanoic acid
a-Linolenic acid (
Linoleic acid ((9Z
Tetradecanoic acid
L-octanoylcarnitin
Dodecanoic acid (
Octanoic acid (cap
N-Acetylneuraminat
Pantothenate
(S)(+)-Allantoin
Creatinine
Homocarnosine
Cytidine
Cytosine
2-Oxoglutarate
Sphinganine 1-phos
3-Sulfocatechol
5-6-Dihydrothymine
D-Rhamnose
Hypoxanthine
acetyl-carnitine (
Heptanoic acid
Hexanoic acid (cap
Octadecanoyl-L-car
D-Arabitol
Indole-3-acetaldeh
Serotonin
D-Ribulose 5-phosp
N-Succinyl-L-glute
Dimethylglycine
GMP
S-Glutathionyl-L-c
gamma-L-Glutamyl-D
5-Hydroxyindoleace
L-methionine
Guanine
L-Methionine S-oxi
Ascorbate
Fumarate
Cys-Gly
AA53-1
AA53-2
AA53-3
AA53-4
AA53-5
AA53-6
AA53-7
AA53-8
AA53-9
AA53-10
AA53-11
AA53-12
AA53-13
AA53-14
D
Polyamine
Glycolysis/TCA
Acyl carnitine
Tryptophan/Indole
Serine biosynthesis
Arginine/proline
Nucleotide metabolism
Signaling
Glycerophospholipid biosynthesis
Hemolysis markers
GSH Homeostasis
Other Sugars
Sphingolipid biosynthesis
Amino acids
Aminosugars
Poly-unsaturated Fatty Acids
Ctrl
USP30I
Cytidine
Serotonin
Hypoxanthine
Dimethylglycine
Creatinine
Cytosine
Acetylcholine
Indole-3-aceta
Homocarnosine
Biliverdin
S-Glutathionyl
D-Arabitol
Cys-Gly
Sphinganine 1-
L-glutamine
N-Acetylneuram
Pyruvate
a-Linolenic ac
5-Hydroxyindol
Fumarate
High
Low
VIP scores